UNDERDAMPED MOTION OF A MICROBEAD IN OPTICAL TWEEZER AND ITS RELATIONSHIP WITH THE REYNOLDS NUMBER

by

VATSAL ASITKUMAR JOSHI

Presented to the Faculty of the Graduate School of
The University of Texas at Arlington in Partial Fulfillment
of the Requirements for the Degree of

MASTER OF SCIENCE
in
MECHANICAL ENGINEERING

THE UNIVERSITY OF TEXAS AT ARLINGTON
December 2018

ACKNOWLEDGEMENTS

I would like to thank my supervising professor Dr. Alan Bowling for constantly motivating and encouraging me. His guidance has helped me during the time of my research. I could not have imagined having a better advisor and a mentor for my master's study. I would also like to thank Dr. Hyejin Moon and Dr. Ashfaq Adnan for being part of my defense committee and providing their time and expertise in reviewing my work.

I would also like to thank Dr. Mahdi Haghshenas-Jaryani for numerous discussions about optical tweezers. I am grateful to my mentors, Dr. Ashley Guy and Abhishek Chatterjee, for invaluable discussions and brainstorming throughout my research. I wish best of luck to my colleagues, Regan Kubicek, Manoochehr Rabiei and Eric Havenhill for their future endeavors.

I am grateful to all the teachers in India and here in the United States of America, especially to thank Dr. David Hullender and Dr. Kamesh Subbarao for igniting my interest in the field of dynamics and controls. I am also very grateful to my school teacher Mr. Santosh Kaushik for making me good at self study which has been very useful in my research.

Finally, I would like to express my deepest gratitude to my parents and my sister who have always encouraged me and have always been supportive. I also thank all of my friends who have helped me throughout my career.

November 15, 2018

ABSTRACT

UNDERDAMPED MOTION OF A MICROBEAD IN OPTICAL TWEEZER AND ITS RELATIONSHIP WITH THE REYNOLDS NUMBER

VATSAL ASITKUMAR JOSHI, M.S.

The University of Texas at Arlington, 2018

Supervising Professor: Alan P. Bowling

Optical tweezers can hold and manipulate microscopic objects with the use of a highly focused laser beam. The radiation pressure acting on the object is generally in the range of piconewtons and can be attractive or repulsive based on the reflective indexes of the object and the surrounding medium. Though the advances in the field of Optical tweezers have been enormous in the past few years, only the object's planer motion can be analyzed with the motion capture technology available today. Due to the wide applications of Optical tweezers in the field of biology and physics, the ability to simulate the motion of these microscopic objects can help gather more data about object's motion and other related characteristics.

One of the major issues related to simulating microscopic objects is the long computation time due to large accelerations. Because the mass of the object is extremely small, even very small amount of force can generate large accelerations resulting in smaller step sizes for numerical integration.

This thesis discusses a method to calculate laser beam force acting on the microscopic object. It also discusses equations of motion of the object. The dispropor-

tionality caused due to large forces and small mass is mostly addressed by the use of famous overdamped Langevin equations, which omit the inertial properties in the equations of motion. However, this first order model is inconsistent with Newton's second law. A method of multiple scales is introduced which solves this problem by bringing all the terms of equations of motion in proportion with each other thus increasing the time step and reducing computation time.

The proposed method was also validated with experiments done on three polystyrene beads with 500nm, 990nm, and 1950nm diameters. A brief discussion is given in the results section about the underdamped behavior of 500nm bead and the significance of low Reynolds number at such small length scale.

TABLE OF CONTENTS

LIST OF ILLUSTRATIONS

LIST OF TABLES

NOMENCLATURE

$\widehat{\mathbf{N}}_i$	Unit vector of inertial frame
$\widehat{\mathbf{P}}_i$	Unit vector of body attached frame
$q_i, \dot{q}_i, \ddot{q}_i$	Generalized coordinate, speed and acceleration
$\mathbf{r}, \dot{\mathbf{r}}, \ddot{\mathbf{r}}$	Bead's position, velocity and acceleration
${}^N\boldsymbol{\omega}^P, {}^N\dot{\boldsymbol{\omega}}^P$	Bead's rotational velocity and rotational acceleration
e_i	Euler Parameter
$\mathbf{e}$	Vector of euler parameters
$\mathbf{p}$	Linear momentum
$\mathbf{F}$	Vector of forces
$\mathbf{M}$	Vector of moments
$\mathbf{H}_{PP}$	Angular momentum of a body about its center of gravity
I_{PP}	Inertia tensor of a body about its center of gravity
A	Mass matrix
$\boldsymbol{\Gamma}$	Generalized active forces
m	Mass of the particle
g	Gravitational acceleration
ρ_m	Density of surrounding medium
V	Volume of fluid displaced
λ_{mfp}	Mean free path
Kn	Knudsen number
β_v	Coefficient of translational drag
β_w	Coefficient of rotational diffusion

$\bar{L}_C$	Characteristic length
μ	Mean value
σ_{st}	Standard deviation
k_B	Boltzmann constant
T	Temperature in kelvin
a	Area
(x_i, y_i)	Coordinates of a point on the objective lens
ρ_i	Radial distance of a point on objective lens from its center
$\mathbf{P}_{AB}$	Position vector from point A to point B
$\widehat{\mathbf{u}}$	Unit direction vector
$I(\rho_i)$	Beam intensity at radial distance ρ_i
σ	Beam waist length
P_t	Total input power
P_i	Power of i^{th} ray
r	Radius of the bead
α_i	Angle of incidence of i^{th} ray
β_i	Angle of refraction of i^{th} ray
R_i, T_i	Fresnel refraction and transmission coefficients of i^{th} ray
n_m	Refractive index of surrounding material
n_P	Refractive index of the bead
c	Speed of light in a vacuum
$F_{sc,i}, F_{gr,i}$	Scattering and gradient force components for i^{th} ray
m_c	Characteristic mass
$\bar{A}$	Modified mass matrix
a_2	Scaling factor

CHAPTER 1

INTRODUCTION

The field of laser-based optical trapping was pioneered by Arthur Ashkin in the early 1970s. In his initial work, he proved that optical forces could displace and levitate micron-sized dielectric particles in both water and air[2], and he developed a stable, three-dimensional trap which required two counter-propagating laser beams[6]. Eventually in 1980s, he developed the single-beam gradient force optical trap[7] which, as the name suggests, used a single laser beam focused by a high numerical aperture microscope objective to trap dielectric particles near the lens focus. This arrangement eventually became known as "Optical Tweezers"[5]. Today, optical tweezers are not only used to hold and manipulate micron and sub-micron sized particles[3], but also to cool and trap neutral atoms[4]. Optical tweezers have been used to probe the viscoelastic properties of cell membranes[20], aggregated protein fibres (such as actin), single biopolymers (such as DNA[27]), composite structures (such as chromatin and chromosomes), and microtubules[28]. The ability to apply forces in the order of a piconewton to micron-sized particles while simultaneously measuring displacement with the precision of a nanometer (or better) is now regularly applied to study physics of colloids[8], molecular motors at the single-molecule level[1], mesoscopic systems, mechanical properties of polymers and biopolymers[19]. Another particular feature of this technique is the possibility to trap individual objects, which can then be studied alone, free from the influence of other objects in the sample.

1.1 Principle of Optical trap

An optical trap is formed when a laser beam is focused with an objective lens of high numerical aperture (NA). A dielectric particle near the focus experiences a force originated due the momentum transfer from the scattering of the laser. This optical force is generally decomposed into two mutually perpendicular force components: (1) a scattering force, in the direction of light propagation and (2) a gradient force, in the direction of the spatial light gradient. Figures 1.1 and 1.2 describes the effect of an trap on a dielectric particle in terms of the total force due to a typical pair of rays R_1 and R_2 of the converging laser beam, under the assumption that the surface of the particle does not reflect light. In this approximation, the forces F_1 and F_2 are entirely due to the momentum change as a result of the refraction of incidenting rays R_1 and R_2. The forces are shown pointing in the direction of the momentum change. Figure 1.1 showcases that for an arbitrary displacement of the particle origin P from the focus f in vertical direction, the magnitude of F_1 and F_2 is same and their vector sum gives a net restoring force F directed back to the focus, and the trap is stable.

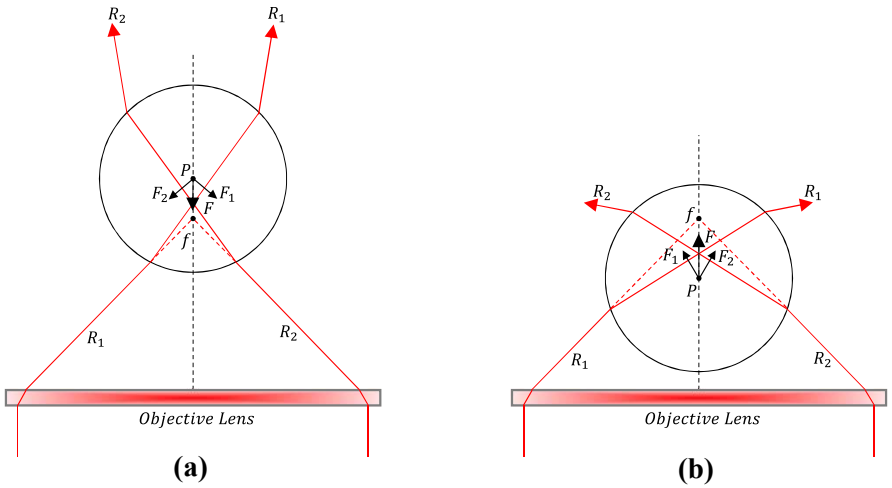

Figure 1.1: Arbitrary displacement of the bead in vertical direction

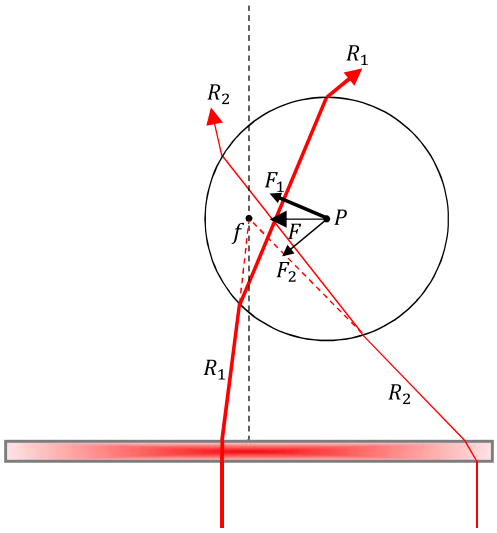

Figure 1.2: Arbitrary displacement of the bead in horizontal direction

Similarly, in Fig. 1.2, for arbitrary displacements of the particle origin P from the focus f in horizontal direction, the magnitude of F_1 and F_2 is different(shown by change in thickness) and their vector sum gives a net restoring force F directed back to the focus. This difference in F_1 and F_2 arises from different intensities of the rays refracting through the particle.

1.2 Motivation and Scope

Requirement of a simulation model for optical tweezers stems from the lack of current technology to provide the data required to analyze the bead's motion. The motion of the bead under the influence of optical forces can be observed in two dimensions only. This becomes a bottleneck in extracting the velocity and acceleration information from the experimental data. A dynamic model representing the bead's motion can be used here to estimate the initial position of the bead in the third

dimension by matching the simulation results with the planar experimental data obtained from the image capturing device.

Majority of studies in this field have investigated the behavior of the bead near the focal line of the optical trap. There studies are mainly focused towards measuring the properties of the optical trap such as axial trap strengths, spring constants and force profiles[15]. However, the implications of the surrounding environment and its effects on the dynamic behavior of the bead during trapping process, under different time and length scales, are not studied adequately. Though, there are some simulation studies done in this field, such as [38] (a Java applet used for teaching purposes), [47] (Simulation of a brownian particle in an optical trap), and a few theoretical studies such as [48] and [35]. However, These simulations assume zero inertia, considering the mass of the bead being extremely small. This results in the first order overdamped Langevin equations which violates Newton's second law of motion.

Reynolds number is defined as the ratio of inertial forces to viscous forces. Furthermore, Reynolds number is directly proportional to the velocity of the fluid with respect to the object. Thus, the Reynolds number for a micrometer-sized object should be very small provided that the velocity is also small. Furthermore, a low Reynolds number would mean that the inertial forces are extremely small as compared to the viscous forces which explain the use of overdamped Langevin equation to model the dynamics of microbead as explained in the previous paragraph. Additionally, it is a well-known theory that micron-sized objects show overdamped behavior while moving through a liquid[39]. However, extrapolating this theory to even smaller sized objects can lead to inaccurate inferences about the dynamic behavior of particles, living cells, and proteins at micro and nanoscales[22, 23, 10, 12].

Experimental and simulation data provided in [26] for the motion of polystyrene beads with different diameters of 500nm, 990nm and 1950nm uses a 2D model. The

experimental and simulation data showed a transition from overdamped to underdamped motion with reduction in the bead diameter. These unconventional results greatly contradicts with the widely accepted notion that a small particle moving in a fluid medium should have low Reynolds number and thus the overdamped motion at the submicron scale. Though, the simulation data matches closely to the experimental data, a planer model was used with some assumptions and approximations.

To address the issues discussed in previous paragraphes, this work introduces a 3D model to simulate the Optical trapping phenomenon. Chapter 2 provides the complete derivation of the equations of motion of the bead and discusses different forces acting on it except the optical forces generated by the laser beam incidenting with the bead. Chapter 3 provides a discussion on the beam discretization and explains how the optical forces can be calculated by using the approach of geometric optics. An established multiple scale analysis has been proven to significantly reduce the computation time required to generate equivalent time histories in continuum regime microscale dynamical simulations by allowing the smallest bodies to be observed from larger time scales. Chapter 4 provides a detailed explanation of this multiple scale analysis. Finally, Chapter 5 discusses the results obtained from the simulations and compares it with experimental data. Chapter 5 also discusses the significance of Reynolds number in the prediction of the dynamic behavior of a bead under the influence of optical tweezers.

CHAPTER 2

DYNAMIC MODEL

The simulations are based on a simple dynamic model of a sphere, here the bead, in a fluid medium. This model is developed using Euler's laws of motion. Figure 2.1 shows the setup for simulation model. The inertial reference point is defined at the center of the objective lens. Inertial reference frame is shown by three unit vectors $\widehat{\mathbf{N}}_1$, $\widehat{\mathbf{N}}_2$ and $\widehat{\mathbf{N}}_3$ mutually perpendicular to each other.

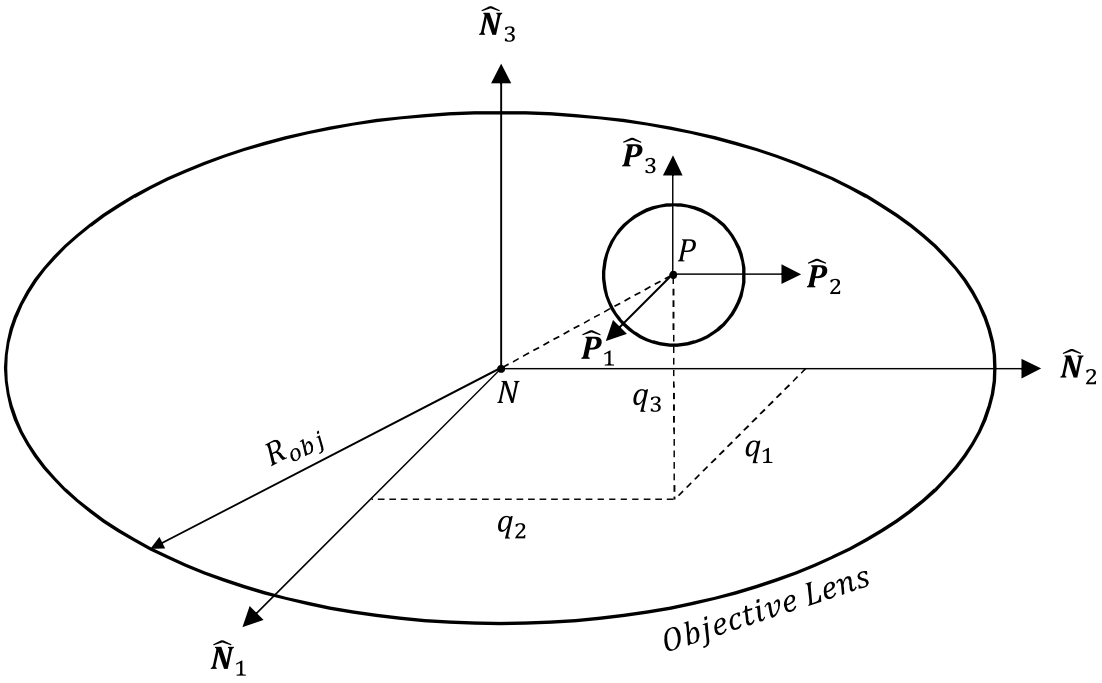

Figure 2.1: 3D model of the system under consideration

The bead is represented as a circle with center P and radius r in the figure. It has a body attached frame with three mutually perpendicular unit vectors $\widehat{\mathbf{P}}_1$, $\widehat{\mathbf{P}}_2$ and

$\widehat{\mathbf{P}}_3$. Bead's position and orientation is defined by three translational coordinates (q_1 through q_3) and four rotational coordinates (e_0 through e_3) as

$$\mathbf{r} = [q_1 \; q_2 \; q_3]^T \qquad\qquad \mathbf{e} = [e_0 \; e_1 \; e_2 \; e_3]^T \tag{2.1}$$

Where, q_1, q_2 and q_3 represent the position of the bead in $\widehat{\mathbf{N}}_1$, $\widehat{\mathbf{N}}_2$ and $\widehat{\mathbf{N}}_3$ directions respectively. While, e_0, e_1, e_2 and e_3 are the euler parameters representing the orientation of the bead. Note that the Euler Angles[9] can be used to compute the rotation matrix. However, any combination of Euler Angles used to compute the rotation matrix always have a singularity. To avoid this problem, Euler Parameters are used which are a set of homogeneous coordinate which will never generate a singular rotation matrix. The generalized translational and rotational speed can be defined as

$$\dot{\mathbf{r}} = \begin{bmatrix} \dot{q}_1 \\ \dot{q}_2 \\ \dot{q}_3 \end{bmatrix} \qquad {}^N\boldsymbol{\omega}^P = \begin{bmatrix} \dot{q}_4 \\ \dot{q}_5 \\ \dot{q}_6 \end{bmatrix} = 2 \begin{bmatrix} -e_1 & e_0 & e_3 & -e_2 \\ -e_2 & -e_3 & e_0 & e_1 \\ -e_3 & e_2 & -e_1 & e_0 \end{bmatrix} \begin{bmatrix} \dot{e}_0 \\ \dot{e}_1 \\ \dot{e}_2 \\ \dot{e}_3 \end{bmatrix} = L\dot{\mathbf{e}} \tag{2.2}$$

Where, $\dot{\mathbf{e}}$ is a vector of the derivatives of Euler parameters. Equation (2.2) provides a relationship between the derivatives of Euler Angles and the angular velocity of the bead. More details about Euler Parameters is provided in Appendix A. Note that $\dot{\mathbf{r}}$ is defined in inertial(N) frame while ${}^N\boldsymbol{\omega}^P$ is defined in body attached(P) frame. The laser beam(not shown here) coming out of objective lens will discussed in detail in Chapter 3.

2.1 Equations of motion

According to Euler's first law of motion, the linear momentum of a body, $\mathbf{p}$, is equal to the product of the mass of the body m and its velocity. So,

$$\mathbf{p} = M\dot{\mathbf{r}} = \begin{bmatrix} m & 0 & 0 \\ 0 & m & 0 \\ 0 & 0 & m \end{bmatrix} \begin{bmatrix} \dot{q}_1 \\ \dot{q}_2 \\ \dot{q}_3 \end{bmatrix} \tag{2.3}$$

where, m is the mass of the bead. Differentiating this equation with respect to time

$$\sum \mathbf{F} = M\ddot{\mathbf{r}} = \begin{bmatrix} m & 0 & 0 \\ 0 & m & 0 \\ 0 & 0 & m \end{bmatrix} \begin{bmatrix} \ddot{q}_1 \\ \ddot{q}_2 \\ \ddot{q}_3 \end{bmatrix} \tag{2.4}$$

Here, $\ddot{\mathbf{r}}$ is the transnational acceleration of the bead's mass-center. Note that equation (2.4) is same as Newton's second law of motion. Forces included on the left-hand side of equation above are discussed in Section 2.2.

According to Euler's second law of motion, the rate of change of angular momentum $\mathbf{H}_{PP}$ about the mass center of the body is equal to the sum of the external moments $\mathbf{M}$ acting on that body about that point. Thus,

$$\sum \mathbf{M} = \frac{d\mathbf{H}_{PP}}{dt} \tag{2.5}$$

$$\frac{d\mathbf{H}_{PP}}{dt} = I_{PP}{}^{N}\dot{\boldsymbol{\omega}}^{P} + {}^{N}\boldsymbol{\omega}^{P} \times \left(I_{PP}{}^{N}\boldsymbol{\omega}^{P}\right) \tag{2.6}$$

Where, I_{PP} is the inertia tensor for the bead, and ${}^{N}\dot{\boldsymbol{\omega}}^{P}$ is the vector of angular accelerations of the bead. Note that equation (2.5) is written completely in body attached frame. Thus, all the moments has to be written in body attached frame. Moments included in $\sum \mathbf{M}$ on the left-hand side of equation (2.5) are discussed in Section 2.2.

The complete system model can be given by combining equations (2.4) and (2.5) and rearranging it into the general form of equations of motion yields

$$A\left(\mathbf{q}\right)\ddot{\mathbf{q}} = \mathbf{\Gamma}\left(\mathbf{q}, \dot{\mathbf{q}}, t\right) \tag{2.7}$$

Where, A is known as the mass matrix, $\ddot{\mathbf{q}}$ is a vector of second order derivatives of the generalized coordinates and $\mathbf{\Gamma}$ is a vector containing all the forces and moments. For the system under consideration, $\ddot{\mathbf{q}}$ and $\mathbf{\Gamma}$ can be defined as

$$\ddot{\mathbf{q}} = [\ddot{q}_1\ \ddot{q}_2\ \ddot{q}_3\ \ddot{q}_4\ \ddot{q}_5\ \ddot{q}_6]^T \qquad\qquad \mathbf{\Gamma}\left(\mathbf{q}, \dot{\mathbf{q}}, t\right) = \begin{bmatrix} \sum \mathbf{F} \\ \sum \mathbf{M} \end{bmatrix} \tag{2.8}$$

Left-hand side of equation (2.7) is known as *generalized inertia forces* and right-hand side is known as *generalized active forces.*

2.2 Forces and Moments

Sum of the forces on the left side of equation (2.4) can be written as

$$\sum \mathbf{F} = \mathbf{F}_g + \mathbf{F}_{buo} + \mathbf{F}_{st} + \mathbf{F}_{drag} + \mathbf{F}_{beam} \tag{2.9}$$

where, $\mathbf{F}_g$, $\mathbf{F}_{buo}$, $\mathbf{F}_{st}$, $\mathbf{F}_{drag}$ and $\mathbf{F}_{beam}$ are gravity, buoyancy, stochastic, drag and laser beam forces respectively. While, sum of the moments on the left side of equation (2.5) can be written as

$$\sum \mathbf{M} = \mathbf{M}_{st} + \mathbf{M}_{drag} + \mathbf{M}_{beam} \tag{2.10}$$

where, $\mathbf{M}_{st}$, $\mathbf{M}_{drag}$ and $\mathbf{M}_{beam}$ are stochastic moment, rotational diffusion and laser beam moments respectively. All except the beam forces and beam moments defined above are discussed in detail in consequent sub-sections.

2.2.1 Gravity and buoyancy

The gravity and buoyancy forces are set as

$$\mathbf{F}_g = -mg\widehat{\mathbf{N}}_3 \tag{2.11}$$

$$\mathbf{F}_{buo} = \rho_m g V \widehat{\mathbf{N}}_3 \tag{2.12}$$

where, g is gravitational acceleration, ρ_m is density of surrounding medium and V is the volume of the surrounding medium displaced by the submerged bead. It is clear from equations (2.11) and (2.12) that the gravitational force act in negative $\widehat{\mathbf{N}}_3$ direction while the force due to buoyancy act in positive $\widehat{\mathbf{N}}_3$ direction. Moments generated due to gravity and buoyancy are zero here and so are not discussed.

2.2.2 Drag

To calculate the drag force acting on the bead, it is important to consider characteristics of the surrounding medium. Knudsen number,Kn, can be used here to determine whether the fluid should be considered as a continuum or as a discrete molecule system. The Knudsen number is defined as the ratio of the mean free path of the molecule of surrounding medium, water here, and the characteristic length of system under observation. The system under consideration has three different bead diameters being 500nm, 990nm and 1950nm. The mean free path of the molecule of surrounding medium is same, $\lambda_{mfp} = 0.3\ nm$, for all three cases. This yields the Knudsen number of 0.0006 for 500nm bead case. Since $Kn = 0.0006$, is less than 0.001, the surrounding medium can be considered as a continuum. An assumption here is that the bead is spherical. Stokes' Law can be used to compute translational drag and the calculations provided in [30] can be used to compute rotational diffusion.

$$\mathbf{F}_{drag} = -\beta_v \left(\dot{q}_1 \widehat{\mathbf{N}}_1 + \dot{q}_2 \widehat{\mathbf{N}}_2 + \dot{q}_3 \widehat{\mathbf{N}}_3 \right) \tag{2.13}$$

$$\mathbf{M}_{drag} = -\beta_\omega{}^N \boldsymbol{\omega}^P = -\beta_\omega L \dot{\mathbf{e}} \tag{2.14}$$

where,

$$\beta_v = 6\pi\mu_m r \qquad and \qquad \beta_\omega = 8\pi\mu_m r^3 \tag{2.15}$$

Where, μ_m is the dynamic viscosity of fluid medium and r is the radius of the bead. It should be noted that the viscous drag and the rotational diffusion acts opposite to the velocity and angular rotation of the bead respectively.

2.2.3 Stochastic forces and moments

Stochastic forces are modeled to represent thermal noise and interactions between modeled and non-modeled bodies. These forces essentially represents Brownian motion. It is modeled as the random forces acting at and the moments acting about the mass center of the bead. They are implemented as Gaussian White noise. The random forces and moments can be defined as

$$\mathbf{F}_{st} = F_{st_1}(t)\widehat{\mathbf{N}}_1 + F_{st_2}(t)\widehat{\mathbf{N}}_2 + F_{st_3}(t)\widehat{\mathbf{N}}_3 \tag{2.16}$$

$$\mathbf{M}_{br} = \bar{L}_C \left(M_{st_1}(t)\widehat{\mathbf{N}}_1 + M_{st_2}(t)\widehat{\mathbf{N}}_2 + M_{st_3}(t)\widehat{\mathbf{N}}_3 \right) \tag{2.17}$$

where, $\bar{L}_C$ represents the characteristic length of the bead. $F_{st_i}(t)$ and $M_{st_i}(t)$ represents the forces and torques respectively, produced by randomly fluctuating molecules of surrounding medium colliding with the bead. Each component of random force or moment is treated independently as a normally distributed random variable[43]. The expectation or mean value of each variable is

$$E\left[F_{st_i}(t)\right] = \langle F_{st_i}(t) \rangle = 0 = \mu \tag{2.18}$$

and the covariance is given by

$$E\left[F_{st_i}(t_1)F_{st_j}(t_2)\right] = \langle F_{st_i}(t_1)F_{st_j}(t_2)\rangle = 2\beta k_B T\delta(t_1 - t_2) \tag{2.19}$$

as provided in [43]. Where, k_b is the Boltzmann constant, T is the absolute temperature of the system in kelvin and β is the drag coefficient. Thus, the variance for each variable can be given as

$$Var(F_{st_i}(t)) = \sigma_{st}^2 = 2\beta k_B T \tag{2.20}$$

Random values of $F_{st_i}(t)$ and $M_{st_i}(t)$ can be generated using the Matlab function `normrnd(`μ`,`σ_{st}`)` which generates random variables with mean μ and standard deviation σ_{st}. Note that $\mathbf{M}_{br}$ in equation (2.17) is written in inertial frame. Thus, $\mathbf{M}_{br}$ has to be converted into a body attached frame.

CHAPTER 3

BEAM MODEL

Beam force calculation for optical trap varies based on the size of the bead relative to the wavelength of light used to trap it. When the size of the bead is much grater than the wavelength of laser beam, calculations based on ray-optics regime are used. On the contrary, if the size of bead is much smaller than the wavelength of laser beam, calculations based on Rayleigh regime are used. In ray-optics regime, the laser beam is discretized into a number of rays, and the approach of geometric optics is used to calculate the forces exerted by each ray on the particle. In the Rayleigh regime, the particle is modeled as a dipole within an electromagnetic field representing the laser beam. There is a third, more generalized, approach known as Generalized Lorenz–Mie theory. With recent advances in this field, it is easy to calculate the beam forces for both smaller and larger diameter particles[36]. Although, it also comes with large computational cost exponentially increasing with the difference in particle size and wavelength. This work uses the ray-optics approach to keep the calculations simple and fast.

3.1 Beam discretization

Figure 3.1 shows a simple planar version of beam model. First, an incident parallel beam of arbitrary mode structure and polarization enters an objective lens situated at the bottom. This beam is then focused at the focal point F by the objective lens. However, the finite size of the actual beam focus can approach $\lambda f/\pi\sigma$[37] where, λ is the wavelength of laser beam, f is the focal length of objective lens and

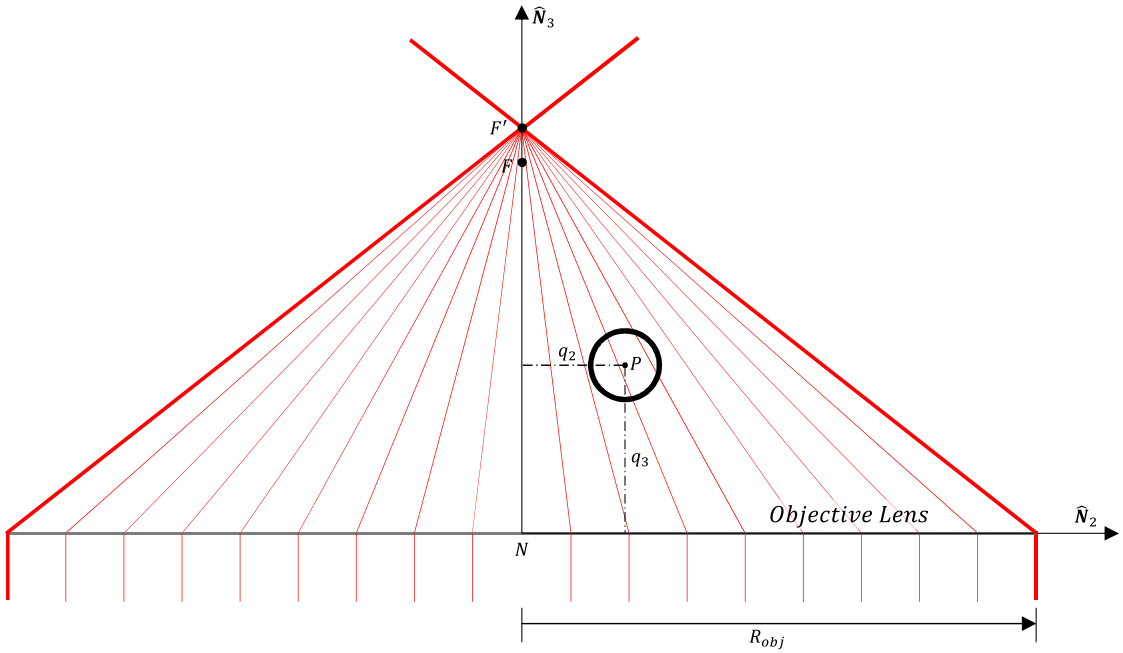

Figure 3.1: Planar beam model

σ is the waist length of the beam at objective lens. The boundary of laser beam, coming out of the objective in $\widehat{\mathbf{N}}_3$ direction, is depicted by thick red lines. The beam discretization is done by dividing the circular area of objective lens into a number of squares as shown in figure 3.2. The area of each square is given by

$$a = \left(\frac{2R_{obj}}{n_{div}}\right)^2 \tag{3.1}$$

where, R_{obj} is the radius of objective lens and n_{div} is the number in which the diameter of objective lens will be divided. The center of each square is considered an origin for the ray. The radial distance of each ray origin form the center of objective lens ρ_i and the unit direction vector $\widehat{\mathbf{u}}_i$ from the ray origin O_i to the focal point F can be computed as

$$\rho_i = \sqrt{x_i^2 + y_i^2} \qquad \widehat{\mathbf{u}}_i = \frac{\mathbf{P}_{O_iF}}{\|\mathbf{P}_{O_iF}\|} \qquad i = 1, 2, 3, \ldots n \tag{3.2}$$

Where, x_i and y_i are the coordinates of ray origins in $\widehat{\mathbf{N}}_1$ and $\widehat{\mathbf{N}}_2$ directions respectively and n is the total number of rays. Ray intensity and power is computed based

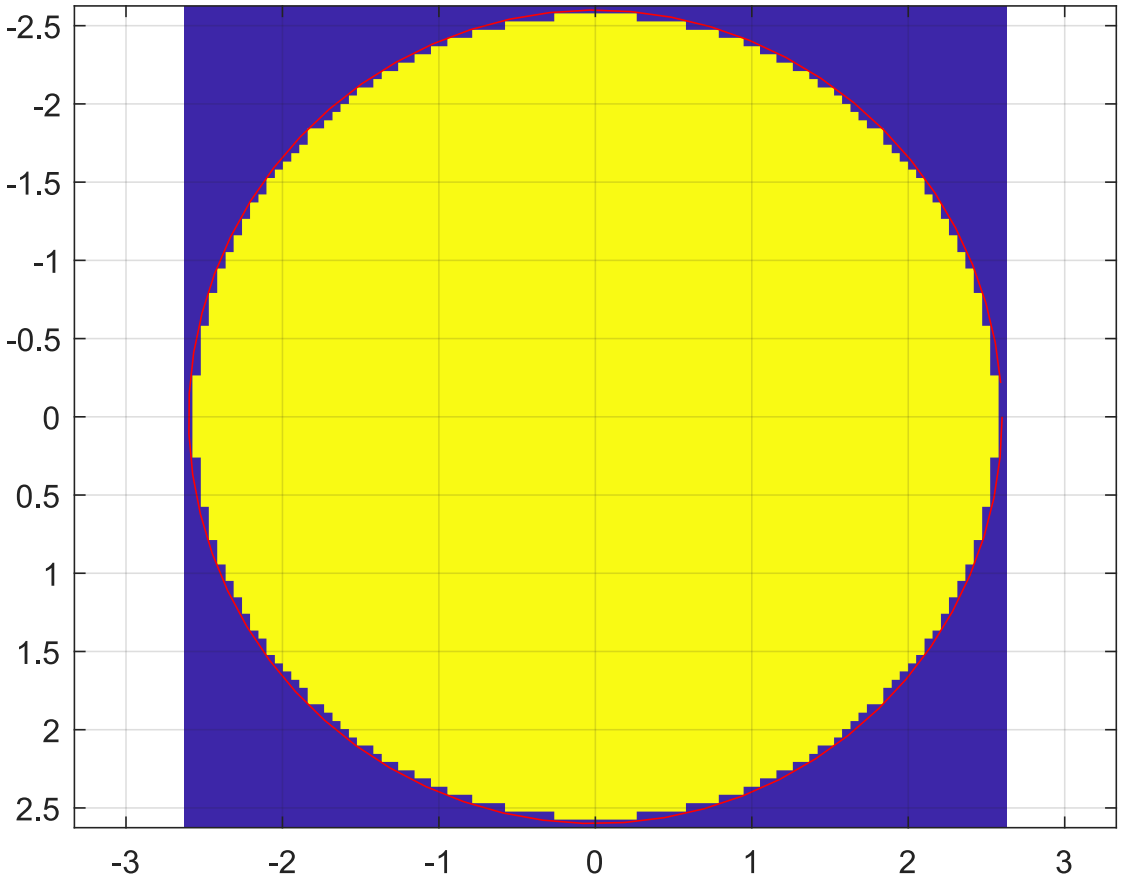

Figure 3.2: Discretization of the surface of objective lens (Red line represents the boundary of objective lens)

on the radial distance ρ_i of each ray origin[40]. The intensity profile, which generally follows the usual Gaussian shape at the objective entrance, can be measured using the techniques given in [45, 46] and can be fitted to the expression

$$I\left(\rho_i\right) = I_0 \exp\left(\frac{-\rho_i^2}{2\sigma^2}\right) \tag{3.3}$$

where, σ is known as the beam waist and I_0 is defined as

$$I_0 = \frac{P_t}{2\pi\sigma^2} \tag{3.4}$$

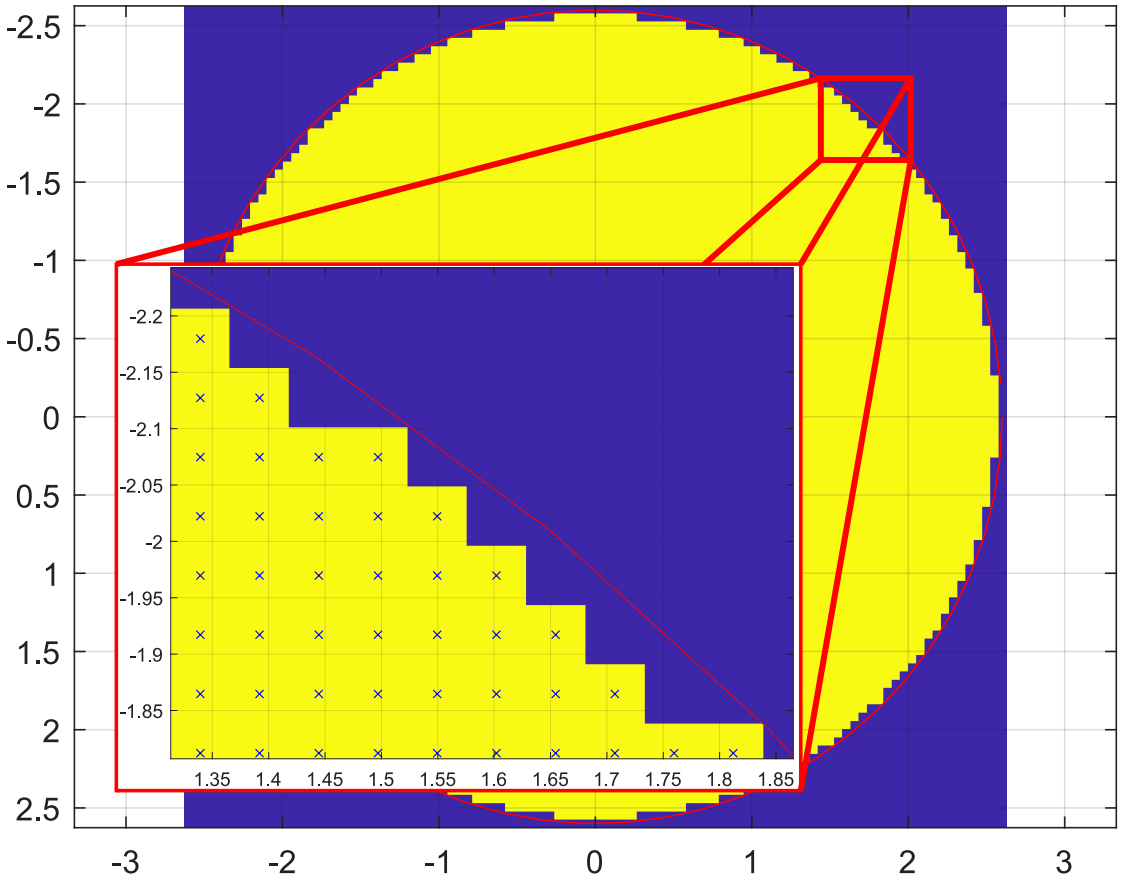

Figure 3.3: Accuracy of the discretization process (Blue × markers show the center of differential area considered as ray origin)

where, P_t is the total beam power. The power of each ray is thus given by following equations

$$P_i = Intensity \cdot Area \tag{3.5}$$

$$\therefore P_i = I\left(\rho_i\right) \cdot a \tag{3.6}$$

$$\therefore P_i = \frac{aP_t}{2\pi\sigma^2} \exp\left(\frac{-\rho_i^2}{2\sigma^2}\right) \tag{3.7}$$

Calculation of the total beam force acting on the bead consists of summing up the contributions of each ray incedenting with the bead.

3.2 Beam force and moments

The optical force calculation given here is adapted from the pioneering work[3] done by Arthur Ashkin, and assumes the bead to be perfectly spherical. It is necessary to do some preliminary calculations before calculating the optical forces. First, the following condition is evaluated to check whether the ray is striking the bead or not.

$$(\widehat{\mathbf{u}}_i \cdot \mathbf{P}_{PO_i})^2 - \|\mathbf{P}_{PO_i}\|^2 + r^2 \geq 0 \tag{3.8}$$

Where, $\mathbf{P}_{PO_i}$ is the position vector from bead center to the ray origin and r is the radius of the bead. If condition (3.8) is true then the ray is striking the bead and further calculations are done. Next step is to calculate the distance between ray origin and a point on the bead where the ray is striking. A line can intersect a sphere at maximum two distinct points. So,

$$d_{1,2} = -\widehat{\mathbf{u}}_i \cdot \mathbf{P}_{PO_i} \pm \sqrt{(\widehat{\mathbf{u}}_i \cdot \mathbf{P}_{PO_i})^2 - \|\mathbf{P}_{PO_i}\|^2 + r^2} \tag{3.9}$$

The point of incident can now be computed as

$$\mathbf{P}_{NC_i} = \mathbf{P}_{NO_i} + \min(d_1, d_2)\, \widehat{\mathbf{u}}_i \tag{3.10}$$

Angle of incidence α_i can now be calculated using the definitions of dot product and cross product.

$$\cos\alpha_i = \frac{\widehat{\mathbf{u}}_i \cdot \mathbf{P}_{PC_i}}{\mathbf{P}_{PC_i}\|} \tag{3.11}$$

$$\sin\alpha_i = \frac{\|\widehat{\mathbf{u}}_i \times \mathbf{P}_{PC_i}\|}{\|\mathbf{P}_{PC_i}\|} \tag{3.12}$$

$$\alpha_i = \tan^{-1}\left(\frac{\sin\alpha_i}{\cos\alpha_i}\right) \tag{3.13}$$

Where, $\mathbf{P}_{PC_i}$ is a vector pointing towards the point of ray incident on the bead (C_i) from bead center P and i represents the ray number. The angle of refraction β_i can be calculated using Snell's law and Pythagorean theorem.

$$\sin\beta_i = \frac{n_m \sin\alpha_i}{n_P} \tag{3.14}$$

$$\cos\beta_i = \sqrt{1 - \sin^2\beta_i} \tag{3.15}$$

$$\beta_i = \tan^{-1}\left(\frac{\sin\beta_i}{\cos\beta_i}\right) \tag{3.16}$$

Where, n_m and n_P are the refractive indexes of surrounding medium and bead respectively. From values calculated above, the Fresnel reflection (R_i) and transmission (T_i) coefficients can be calculated as

$$R_i = \frac{1}{2}\left[\left(\frac{n_m\cos\alpha_i - n_P\cos\beta_i}{n_m\cos\alpha_i + n_P\cos\beta_i}\right)^2 + \left(\frac{n_m\cos\beta_i - n_P\cos\alpha_i}{n_m\cos\beta_i + n_P\cos\alpha_i}\right)^2\right] \tag{3.17}$$

$$T_i = 1 - R_i \tag{3.18}$$

Figures 3.4 and 3.5 show how the optical forces are generated when a ray of power P_i hits a dielectric sphere at an angle of incidence (α_i) with incident momentum of $n_m P_i/c$ per second. The total force acting on the bead is the sum of contributions due to the reflected ray of power $P_i R_i$ and the infinite number of emergent refracted rays of successively decreasing power $P_i T_i^2$, $P_i T_i^2 R_i \ldots$, $P_i T_i^2 R_i^n$. The quantities R_i and T_i are the corresponding Fresnel reflection and transmission coefficients of the bead surface at α_i. The net force acting through the bead's mass-center P can be resolved into scattering force ($F_{sc,i}$) and gradient force ($F_{gr,i}$) components as given by Roosen et al. (see Refs. [41, 42]):

$$F_{sc,i} = \frac{n_m P_i}{c}\left[1 + R_i\cos 2\alpha_i - a_i\right] \tag{3.19}$$

where,

$$a_i = \frac{T_i^2 \left[\cos(2\alpha_i - 2\beta_i) + R_i \cos 2\alpha_i\right]}{1 + R_i^2 + 2R_i \cos 2\beta_i} \tag{3.20}$$

and

$$F_{gr,i} = \frac{n_m P_i}{c} \left[R_i \sin 2\alpha_i - b_i\right] \tag{3.21}$$

where,

$$b_i = \frac{T_i^2 \left[\sin\left(2\alpha_i - 2\beta_i\right) + R_i \sin 2\alpha_i\right]}{1 + R_i^2 + 2R_i \cos 2\beta_i} \tag{3.22}$$

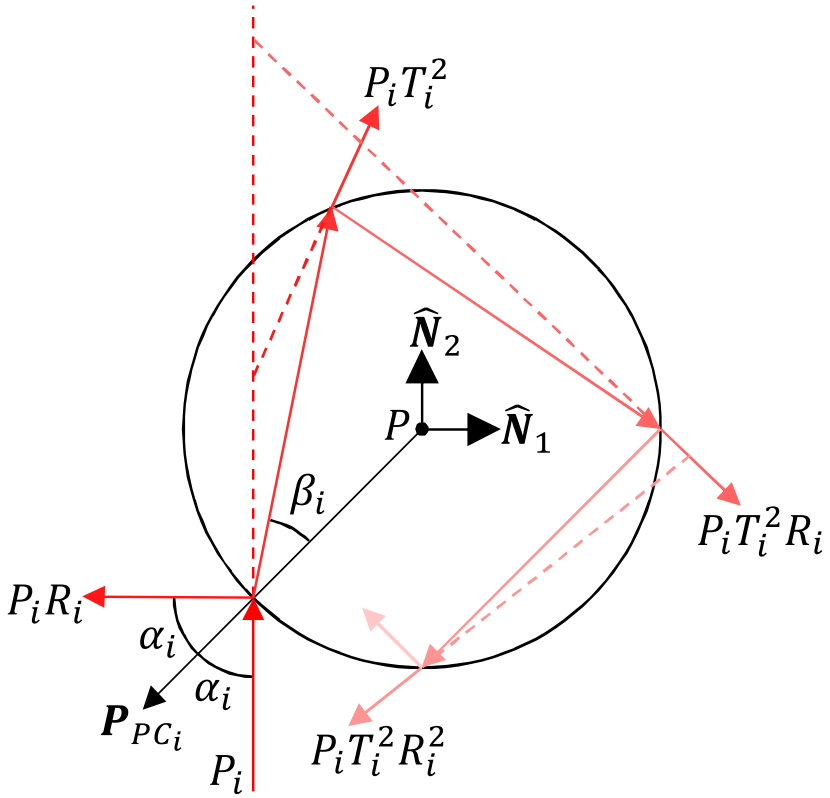

Figure 3.4: Geometry for calculating the force imparted by a single incident ray and its internal reflections

Where, α_i and β_i are the angle of incidence and angle of refraction for one ray. These formulas sum the contribution of all the scattered rays, and are therefore exact. Since R_i and T_i are different for rays polarized perpendicular or parallel to the plane of incidence, the forces are polarization dependent. It should be noted that this calculation is for just one ray. Equations (3.19) and (3.21) provide us with the amount of scattering and gradient force acting on the bead by one ray. However, it does not tell anything about the direction of these forces. As explained in [3], the scattering force component ($F_{sc,i}$) acts in the direction parallel to the incident ray (see Fig. 3.5). While, the gradient force component ($F_{gr,i}$) acts perpendicular to the ray axis pointing in the direction from bead's mass-center to ray axis (see Fig. 3.5). Scattering force ($F_{sc,i}$) thus acts in $\widehat{\mathbf{u}}_i$ direction. Gradient force direction can be computed as

$$\widehat{\mathbf{n}}_i = \frac{\mathbf{P}_{PO_i} + (\widehat{\mathbf{u}}_i \cdot \mathbf{P}_{O_iP})\,\widehat{\mathbf{u}}_i}{\|\mathbf{P}_{PO_i} + (\widehat{\mathbf{u}}_i \cdot \mathbf{P}_{O_iP})\,\widehat{\mathbf{u}}_i\|} \tag{3.23}$$

In the equation above, $\widehat{\mathbf{n}}_i$ essentially represents a unit vector pointing towards a point on ray axis which is closest to the center of the bead. Thus, the action of scattering force is to push the bead in the direction of ray and the action of gradient force is to pull the center of the bead towards ray axis. Thus, the force vectors in inertial frame can be computed as follows,

$$\mathbf{F}_{beam,i} = F_{sc,i}\widehat{\mathbf{u}}_i + F_{gr,i}\widehat{\mathbf{n}}_i \tag{3.24}$$

Each $\mathbf{F}_{beam,i}$ is acting at the corresponding point of incidence C_i. Moment generated by each ray is thus

$$\mathbf{M}_{beam,i} = \mathbf{P}_{PC_i} \times \mathbf{F}_{beam,i} \tag{3.25}$$

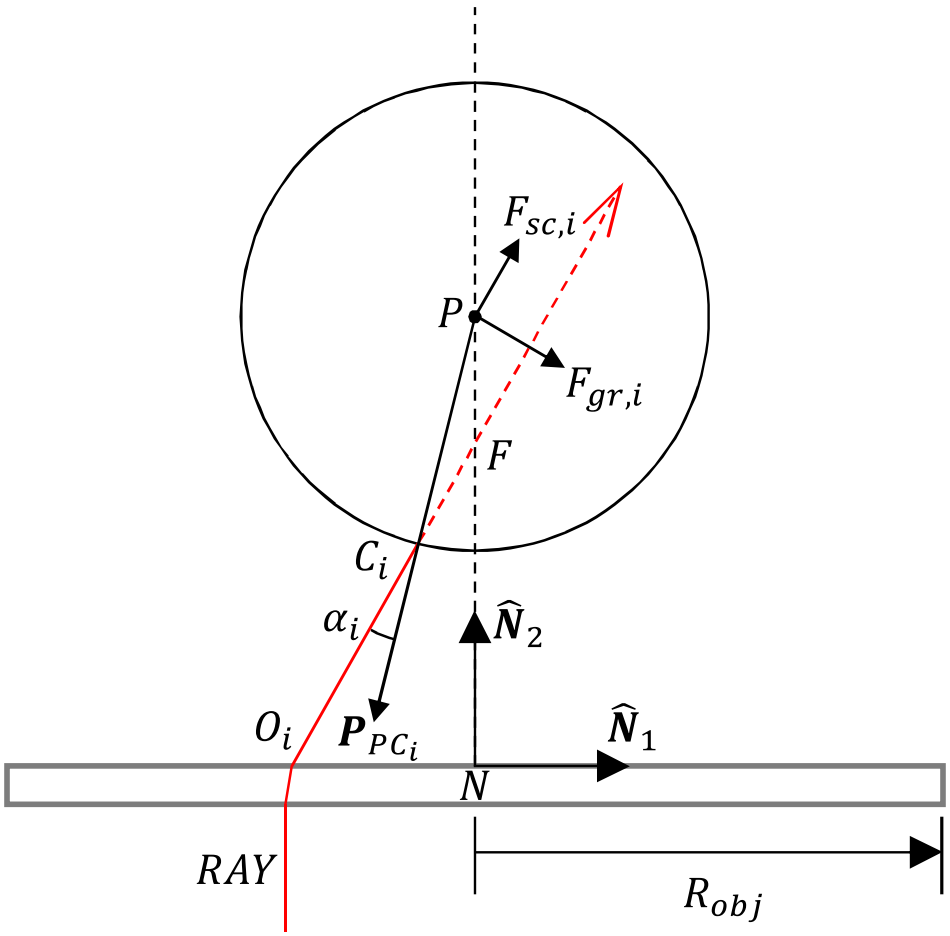

Figure 3.5: Geometry of an incident ray giving rise to gradient and scattering force components

Total optical force and moment of the whole beam is defined as the vector sum of the force and moment contributions of each individual ray within the beam as

$$\mathbf{F}_{beam} = \sum_{i=1}^{n} \mathbf{F}_{beam,i} \qquad \mathbf{M}_{beam} = \sum_{i=1}^{n} \mathbf{M}_{beam,i} \tag{3.26}$$

CHAPTER 4

MULTI-SCALE ANALYSIS

In Chapter 3, the equations of motion are generated, step-wise, including the discussion on how to calculate different forces acting on the bead. However, a key issue originates when these equations are numerically integrated. The integration step size becomes extremely small. Small mass of the bead and large drag force play a big role here. At such a small scale, inertia of the bead is very small as compared to drag forces until and unless the acceleration is extremely high. This imbalance between the scales of inertia and other forces makes numerical integrator to reduce step size in order to keep relative error within acceptable tolerance.

In order to analyze this issue properly, it is necessary to analyze the relationship between generalized inertia and viscous drag forces and moments. Consider the general form of the equations of motion,

$$A(\mathbf{q})\,\ddot{\mathbf{q}} = \mathbf{\Gamma}(\mathbf{q}, \dot{\mathbf{q}}, t) \tag{4.1}$$

Splitting $\mathbf{\Gamma}(\mathbf{q}, \dot{\mathbf{q}}, t)$ in two parts as

$$\mathbf{\Gamma}(\mathbf{q}, \dot{\mathbf{q}}, t) = \mathbf{\Gamma}_{drag}(\dot{\mathbf{q}}) + \mathbf{\Gamma}_{others}(\mathbf{q}, t) \tag{4.2}$$

where, $\mathbf{\Gamma}_{others}(\mathbf{q}, t)$ is the sum of all generalized active forces except viscous drag. Viscous drag $\mathbf{\Gamma}_{drag}(\dot{\mathbf{q}})$ is defined as

$$\mathbf{\Gamma}_{drag} = -\beta D\dot{\mathbf{q}} \tag{4.3}$$

The term $-\beta D\dot{\mathbf{q}}$ in equation above models the friction forces where β is a scalar characteristic damping term and D is matrix that maps the friction to the generalized speeds. Equation (4.1) can be rearranged as

$$m_c \bar{A}\left(\mathbf{q}\right)\ddot{\mathbf{q}} + \beta D\dot{\mathbf{q}} = \mathbf{\Gamma}_{others}\left(\mathbf{q}, t\right) \tag{4.4}$$

where, m_c is a characteristic mass term that has been extracted from A leaving the modified $\bar{A}$ term. Normalizing equation (4.4) by the damping term β yields

$$\frac{m_c}{\beta}\bar{A}\left(\mathbf{q}\right)\ddot{\mathbf{q}} + D\dot{\mathbf{q}} = \frac{\mathbf{\Gamma}_{others}\left(\mathbf{q}, t\right)}{\beta} \tag{4.5}$$

For 500nm bead, the inertia properties are $m = 0.0687$ pg and $I_{PP} = 0.00173 \times 10^{-6}$ pg·mm^2. As discussed in Chapter 2, Stokes' law is used to calculate the translational drag coefficient as $\beta_v = 6\pi\mu_m r = 4.722 \times 10^3$pg/ms. The rotational drag coefficient is calculated using an analysis of rotational diffusion [30] as $\beta_\omega = 8\pi\mu_m r^3 = 3.935 \times 10^{-4}$ pg·mm^2/ms, where r is the radius of the bead, and μ_m is the viscosity of the fluid medium. Considering bead's mass and translational drag coefficient to be characteristic mass and damping terms in equation (4.5) yields

$$\frac{m_c}{\beta}\bar{A}\left(\mathbf{q}\right)\ddot{\mathbf{q}} + D\dot{\mathbf{q}} = \left(1.455 \times 10^{-5}\right)\bar{A}\left(\mathbf{q}\right)\ddot{\mathbf{q}} + D\dot{\mathbf{q}} = \frac{\mathbf{\Gamma}_{others}\left(\mathbf{q}, t\right)}{\beta} \tag{4.6}$$

From the calculation above, it is clear that the disproportionality between mass and drag coefficients is in the order of 10^{-5} which creates large accelerations resulting in smaller integration time step yielding a long numerical integration time.

One solution suggested to reduce the run time is to neglect acceleration term in equations of motion due to small coefficient[39]. This is the basis for overdamped Langevin equation. However, neglecting acceleration yields a first order model which has limitations like overdamped motion of the object or the generalized active force being directly proportional to velocity of the object. Though this approach gives

quicker results, it clearly violates Newton's second law of motion. Other methods for tackling multi-scale problems can be classified as serial and concurrent approaches. Serial approaches separate the whole system into several subsystems defined at varying resolution[29]. These systems are arranged in a hierarchical manner where system states with higher resolution are used to define inputs for medium-resolution systems, which are, in turn, used to calculate the inputs for systems with lower resolution. These formulations are useful for studies in which properties are easily described by scale[49]. Instead, concurrent methods tackle this problem by combining all the simulation layers and sharing the information between them[13]. These formulations have found extensive use in material studies[31] and investigations of crack propagation[14, 44].

Another approach that can solve this problem is the multiple-scale analysis, which comprises the techniques used to construct uniformly valid approximations to the solutions of perturbation problems[33]. This is done by first modeling all bodies together. Then reformulating the equations of motion by defining a characteristically small number from the model, $m_c/\beta = \varepsilon \approx 1.455 \times 10^{-5}$ in this case, which can be used to scale the generalized active forces such that they do not produce large accelerations, but do yield an accurate estimate of the system's motion. Substituting this number in equation (4.6) yields

$$\mathbf{0} = \varepsilon \bar{A}\left(\mathbf{q}\right) \ddot{\mathbf{q}} - \frac{\mathbf{\Gamma}_{others}\left(\mathbf{q}, t\right)}{\beta} + D\dot{\mathbf{q}} \tag{4.7}$$

This small parameter ε is used to introduce the slower time scales as

$$T_0 = \varepsilon^0 t \qquad T_1 = \varepsilon^1 t \qquad T_2 = \varepsilon^2 t \qquad \ldots \qquad T_n = \varepsilon^n t \tag{4.8}$$

The time derivatives $\dot{\mathbf{q}}$ and $\ddot{\mathbf{q}}$ can now be expanded into an asymptotic series as

$$\dot{\mathbf{q}} = \frac{d\mathbf{q}}{dt} = \varepsilon^0 \frac{\partial \mathbf{q}}{\partial T_0} + \varepsilon^1 \frac{\partial \mathbf{q}}{\partial T_1} + \varepsilon^2 \frac{\partial \mathbf{q}}{\partial T_2} + \ldots \tag{4.9}$$

and

$$\ddot{\mathbf{q}} = \frac{d^2\mathbf{q}}{dt^2} = \sum_{i=0}^{\infty}\sum_{j=0}^{\infty} \varepsilon^i \varepsilon^j \frac{\partial^2 \mathbf{q}}{\partial T_i \cdot \partial T_j} \tag{4.10}$$

Substituting these expansions into equation (4.7) and rearranging the terms in the increasing order of ε yields

$$\mathbf{0} = \varepsilon^0 \left(D\frac{\partial \mathbf{q}}{\partial T_0} - \frac{\mathbf{\Gamma}_{others}\left(\mathbf{q}, t\right)}{\beta} \right) + \varepsilon^1 \left(\bar{A}\left(\mathbf{q}\right) \frac{\partial^2 \bar{\mathbf{q}}}{\partial T_0^2} + D\frac{\partial \mathbf{q}}{\partial T_1} \right) + \ldots \tag{4.11}$$

Note that the first term on the right side of equation (4.11) contains all generalized active forces. The second term contains generalized inertia forces and the first set of higher order terms. Considering how ε is defined, the difference between $\varepsilon^0 = 1$ and $\varepsilon^1 = 1.455 \times 10^{-5}$ is fairly large, and so, it is necessary for the first term to largely cancel if the right side of equation (4.11) is equal to zero. From the standpoint of multibody dynamics, if forces cancel each other, they do no work and produce no motion. Such forces can thus be omitted from equations of motion. Note that this claim assumes that the accelerations are not significantly large.

Often in truth "Newton-Euler" models, the assumption given above is untrue due to the first term in equation (4.11) being not equal to zero resulting in large accelerations. These accelerations can be oscillatory, requiring small integration step sizes to resolve; but ultimately do not contribute to the overall motion of the object. This oscillatory behavior is more evident in case of higher-resolution or atomistic models[21], but is still preset in lower resolution models[11, 25] and is often the result of stiff behavior of the system. The multiple-scales formulation shown here imposes the assumption of small accelerations by scaling the generalized active forces.

The scaling of the generalized active forces is achieved by decomposing the first term of equation (4.11) into small and large parts as

$$\varepsilon^0 \left(D\frac{\partial \mathbf{q}}{\partial T_0} - \frac{\mathbf{\Gamma}_{others}\left(\mathbf{q}, t\right)}{\beta} \right) = \left(a_1 + a_2\right) \left(D\frac{\partial \mathbf{q}}{\partial T_0} - \frac{\mathbf{\Gamma}_{others}\left(\mathbf{q}, t\right)}{\beta} \right) \tag{4.12}$$

where, $a_1 + a_2 = \varepsilon^0 = 1$ and $a_1 \gg a_2$. Substituting equation (4.12) back into equation (4.11) yields

$$\begin{aligned}\mathbf{0} =& a_1 \left(D\frac{\partial \mathbf{q}}{\partial T_0} - \frac{\mathbf{\Gamma}_{others}\left(\mathbf{q},t\right)}{\beta} \right) + a_2 \left(D\frac{\partial \mathbf{q}}{\partial T_0} - \frac{\mathbf{\Gamma}_{others}\left(\mathbf{q},t\right)}{\beta} \right) \\ &+ \varepsilon^1 \left(\bar{A}\left(\mathbf{q}\right) \frac{\partial^2 \bar{\mathbf{q}}}{\partial T_0^2} + D\frac{\partial \mathbf{q}}{\partial T_1} \right) + \dots \end{aligned} \tag{4.13}$$

As discussed, the assumption here is that the large part of generalized active forces $\mathbf{\Gamma}\left(\mathbf{q}, \dot{\mathbf{q}}, t\right)$ cancel to the extent that it can be removed from equation (4.13), yielding a second-order model of the form

$$\mathbf{0} = a_2 \left(D\frac{\partial \mathbf{q}}{\partial T_0} - \frac{\mathbf{\Gamma}_{others}\left(\mathbf{q},t\right)}{\beta} \right) + \varepsilon^1 \left(\bar{A}\left(\mathbf{q}\right) \frac{\partial^2 \bar{\mathbf{q}}}{\partial T_0^2} + D\frac{\partial \mathbf{q}}{\partial T_1} \right) + \dots \tag{4.14}$$

$$\therefore \mathbf{0} = A\left(\mathbf{q}\right)\ddot{\mathbf{q}} - a_2 \mathbf{\Gamma}_{others}\left(\mathbf{q},t\right) + a_2 \beta D\dot{\mathbf{q}} \tag{4.15}$$

$$\therefore A\left(\mathbf{q}\right)\ddot{\mathbf{q}} + a_2 \beta D\dot{\mathbf{q}} = a_2 \mathbf{\Gamma}_{others}\left(\mathbf{q},t\right) \tag{4.16}$$

Remember that this equation uses ${}^N\dot{\boldsymbol{\omega}}^P$ and ${}^N\boldsymbol{\omega}^P$ defined in body attached frame. To implement Euler parameters, equation (4.16) can be rewritten as following using the calculation procedure provided in Appendix A.

$$\begin{bmatrix} A_{(3\times3)} & 0_{(3\times4)} \\ 0_{(4\times3)} & \widetilde{I}_{(4\times4)} \end{bmatrix} \begin{bmatrix} \ddot{\mathbf{q}} \\ \ddot{\mathbf{e}} \end{bmatrix} = \begin{bmatrix} a_2 \sum \mathbf{F}_{(3\times1)} \\ \widetilde{\mathbf{M}}_{(4\times1)} \end{bmatrix} \tag{4.17}$$

where,

$$\widetilde{I}_{(4\times4)} = \begin{bmatrix} I_{\mathrm{AA}} L \\ \mathbf{e}^{\mathrm{T}} \end{bmatrix} \qquad \widetilde{\mathbf{M}}_{(4\times1)} = \begin{bmatrix} a_2 \sum \mathbf{M} - \mathbf{K} \\ -\dot{\mathbf{e}}^{\mathrm{T}}\dot{\mathbf{e}} \end{bmatrix} \tag{4.18}$$

Here, $\mathbf{e}$, $\dot{\mathbf{e}}$ and $\ddot{\mathbf{e}}$ are the Euler Parameters and their derivatives. This scaled equation of motion, equation (4.18), suggests that if the system satisfies the condition of low acceleration values, the generalized active forces can be scaled by the small parameter a_2. The value of a_2 is user-specified and found by comparing scaled and unscaled

response for short-time simulations. A useful first guess is $a_2 \approx \varepsilon$. This force scaling can also be used to eliminate the high frequency accelerations of a system that require small time steps for integration. This allows for the integration to be performed at larger time steps, usually an order of magnitude increase. By increasing the integration time step, the number of integration steps that must be performed is reduced, which in turn reduces the real time required to generate the time evolution data.

CHAPTER 5

RESULTS AND DISCUSSION

Simulations were run for each of the three bead diameters, 500nm, 990nm and 1950nm respectively, using the calculations discussed in Chapter 2 through 4. All simulations were coded using MATLAB programming language. Numerical integration was performed on an HP Z230 workstation with a quad-core 3.2GHz Intel Xeon processor running Windows 10 operating system. The integration was performed by a variable time step Dormand-Prince algorithm[16] provided as `ode45` in MATLAB. Relative and absolute errors were 10^{-7} and 10^{-8} respectively. The laser beam was discretized in 7645 rays. A unit system of (pg, mm, ms) was used to keep the order of terms in the equations of motion close to each other for all three cases. Simulation parameters for each case are provided in Tables B.1 through B.4. Subsequent sections discuss different aspects of the results obtained from simulations.

5.1 Experimental and simulation results

The results obtained from the experiments and simulations for the bead's motion in $\widehat{\mathbf{N}}_2$ direction with respect to time are shown in the figures 5.1 through 5.3 for all three beads. It can be observed that while some variance is present, the simulation and experimental results are mostly consistent. One of the goals of this work was to estimate the initial position of the bead in $\widehat{\mathbf{N}}_3$ direction as discussed earlier in Section 1.2. The measured initial values in $\widehat{\mathbf{N}}_1$ and $\widehat{\mathbf{N}}_2$ direction and estimated values in $\widehat{\mathbf{N}}_3$ direction are provided in table 5.1. All values are in meters.

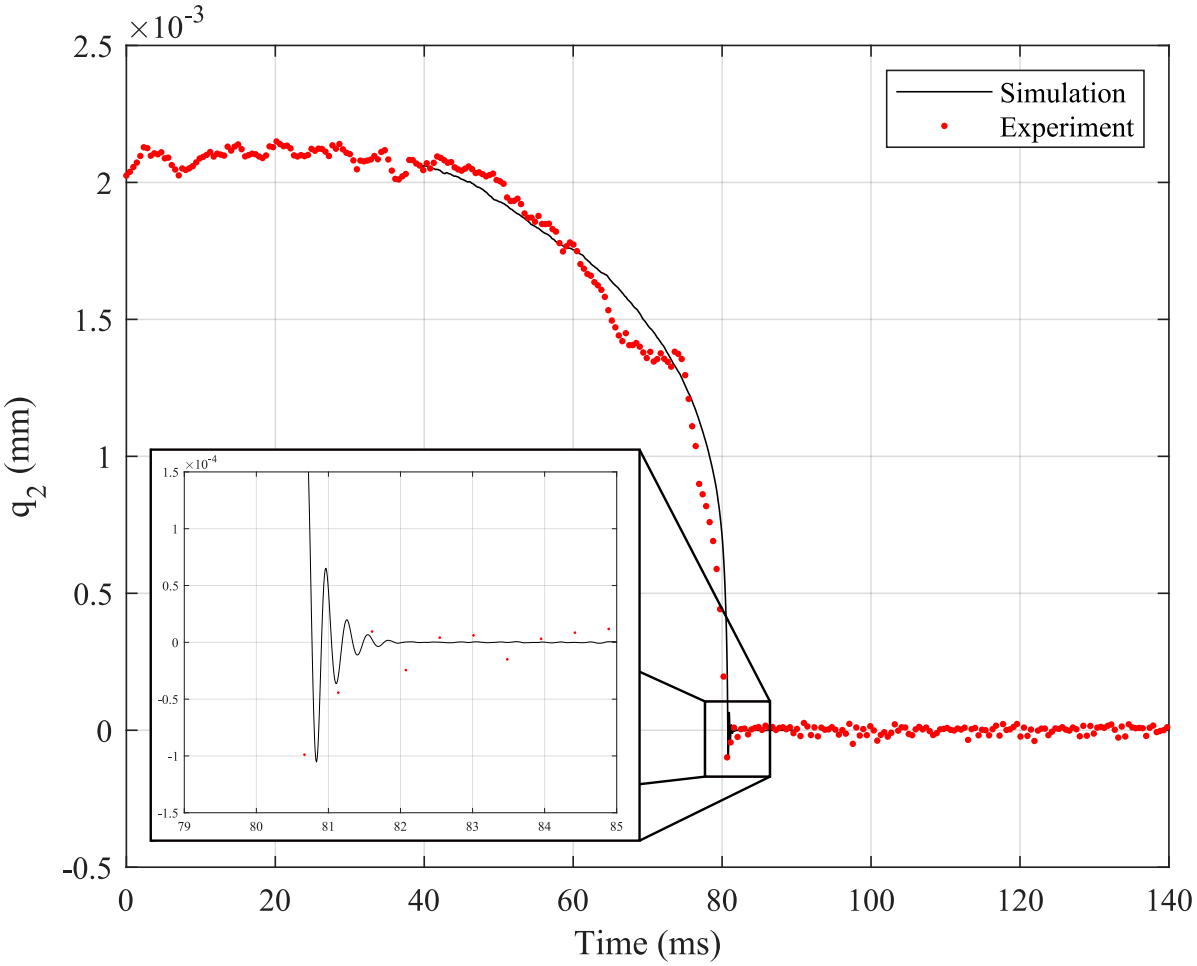

Figure 5.1: Comparison of experimental data (dots) and simulation data (line) for q_2 coordinate of 500nm microbead using the multiscale model

Bead Diameter	$\widehat{\mathbf{N}}_1$	$\widehat{\mathbf{N}}_2$	$\widehat{\mathbf{N}}_3$
500nm	0	2.0616×10^{-6}	1.99795×10^{-3}
990nm	0	-2.045×10^{-6}	1.99595×10^{-3}
1950nm	0	3.4043×10^{-6}	1.9929×10^{-3}

Table 5.1: Initial conditions

The overdamped motion of the largest bead, 1950nm, can be observed in figure 5.3 for simulation results and it matches with the experimental results. However, this overdamped behavior gradually becomes underdamped in the experimental and

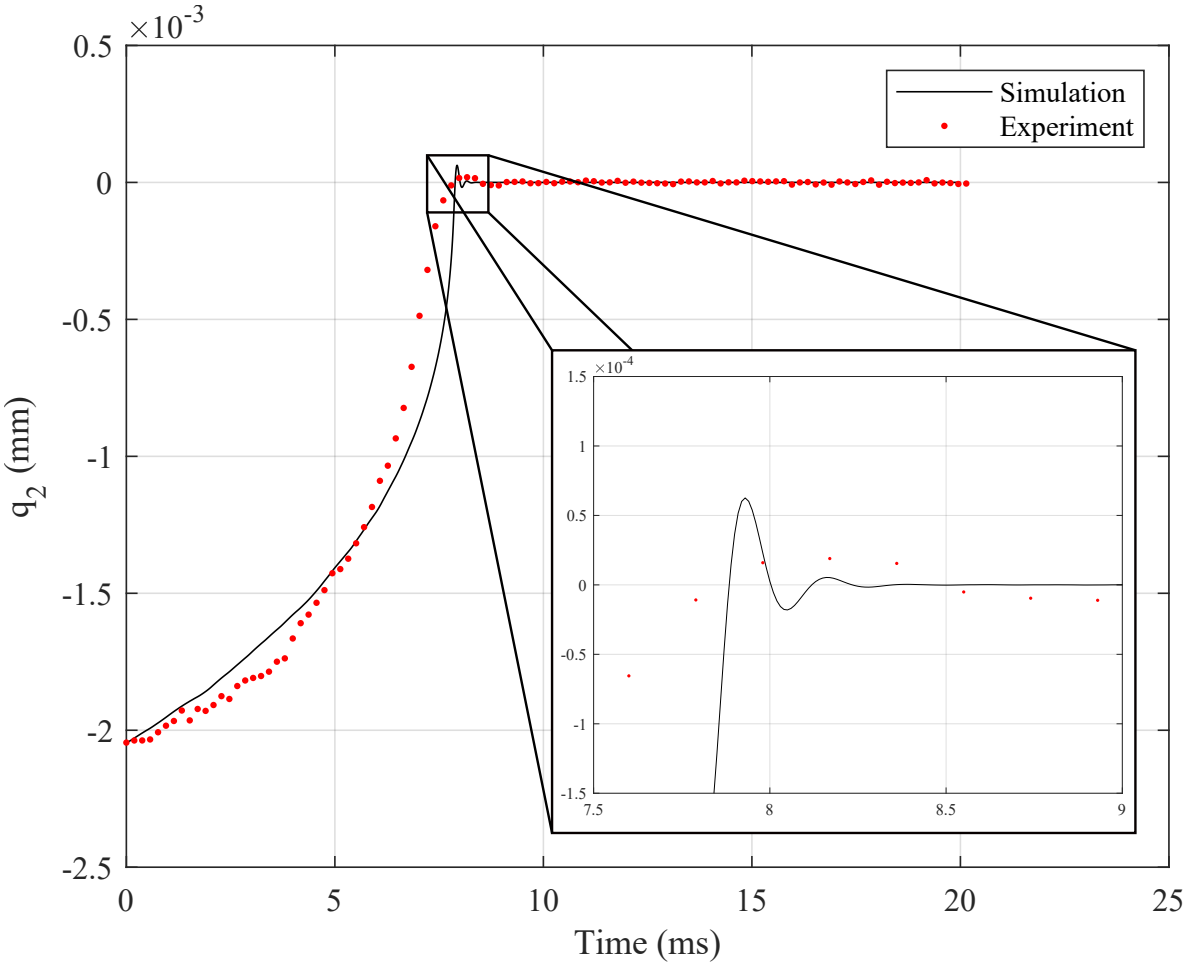

Figure 5.2: Comparison of experimental data (dots) and simulation data (line) for q_2 coordinate of 990nm microbead using the multiscale model

simulation results as the bead size reduces. The 990nm bead shows a small overshoot beyond the focal line and oscillates to a small extent before settling. The simulation result, solid line, shows that these small oscillations can be predicted by the multi-scale model by the proper tuning of the scaling parameter, a_2. The smallest bead, 500nm, shows a much larger overshoot near the focal line with larger oscillations. This concludes that the oscillatory behavior of the bead is dependent on the size of the bead as predicted by the proposed model ; Smaller the size of the bead , larger the oscillatory behavior and vice versa. Note that the underdamped behavior was also

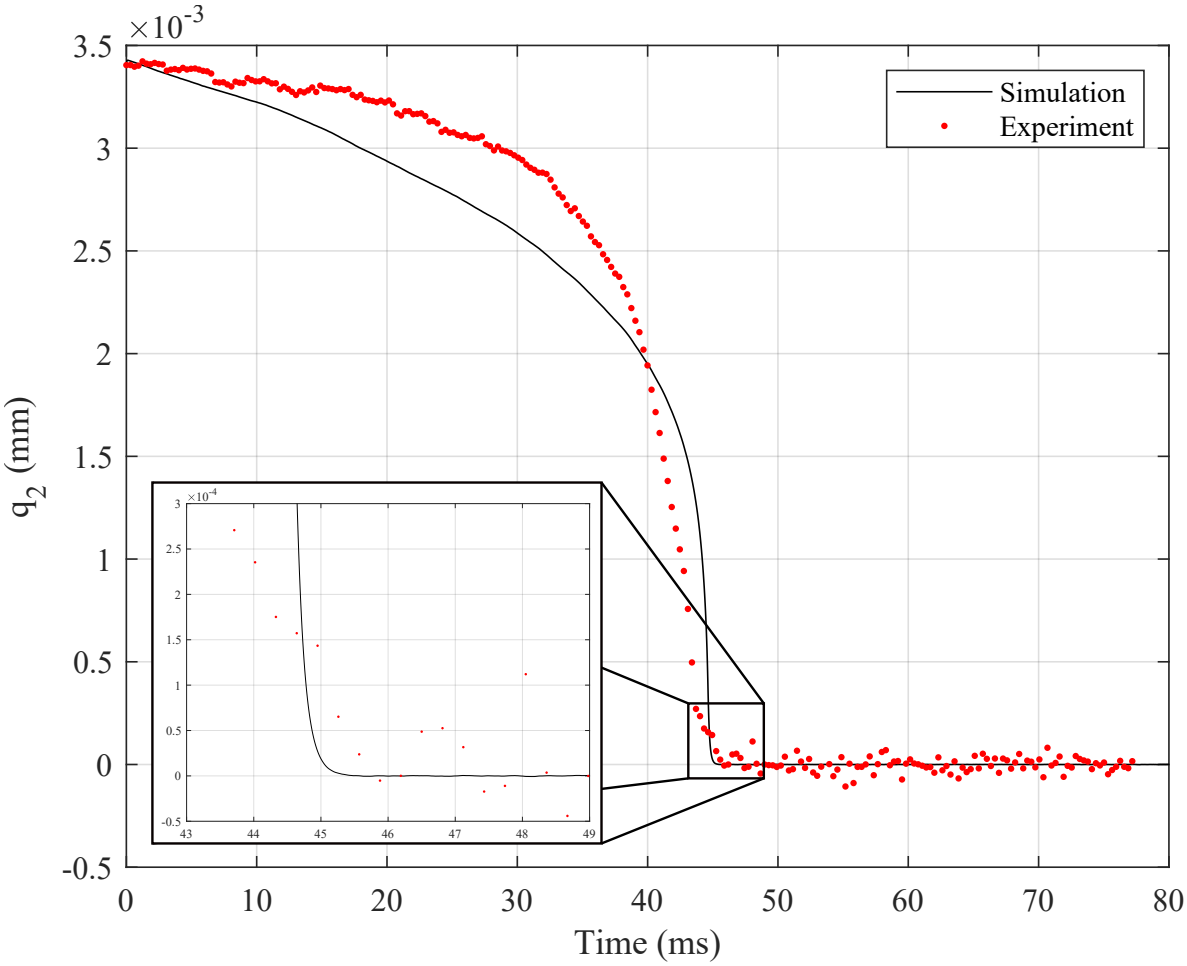

Figure 5.3: Comparison of experimental data (dots) and simulation data (line) for q_2 coordinate of 1950nm microbead using the multiscale model

observed in a theoretical investigation of a micro-optic cubic glass structure which also fllowed the ray-optics approach[17]. Extra position and rotation data available from the simulations is provided in Appendix C for the sake of completeness.

5.2 Reynolds number

The Reynolds number given by following equation

$$Re = \frac{2\rho_m v r}{\mu_m} \tag{5.1}$$

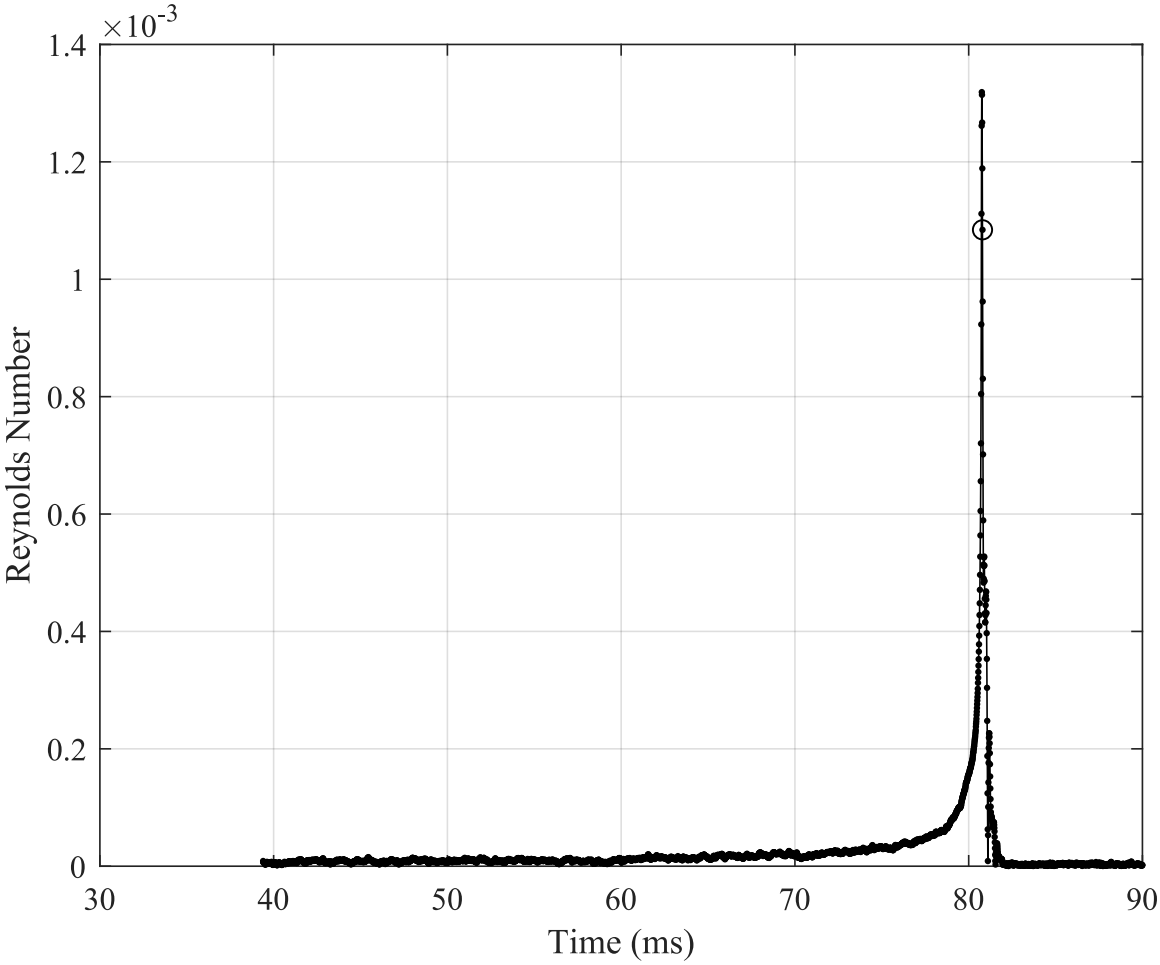

Figure 5.4: Raynolds number versus time for 500nm bead (the marker ◯ indicate the first closest approach (FCA) to the focal point)

is in the order of $10^{-9} \leq Re \leq 10^{-3}$ for all three simulations discussed in previous section. Where, ρ_m is the density of the fluid medium, v is the relative velocity of the object and the fluid, and μ_m is the dynamic viscosity of the fluid medium. The computed values of the Reynolds number over time are plotted in figures 5.4 through 5.6.

A low Reynolds number implies that the viscous forces have a much larger effect on the bead's motion than the inertial forces. In other words, the effects of viscosity are much more important than those of momentum, which should yield the appear-

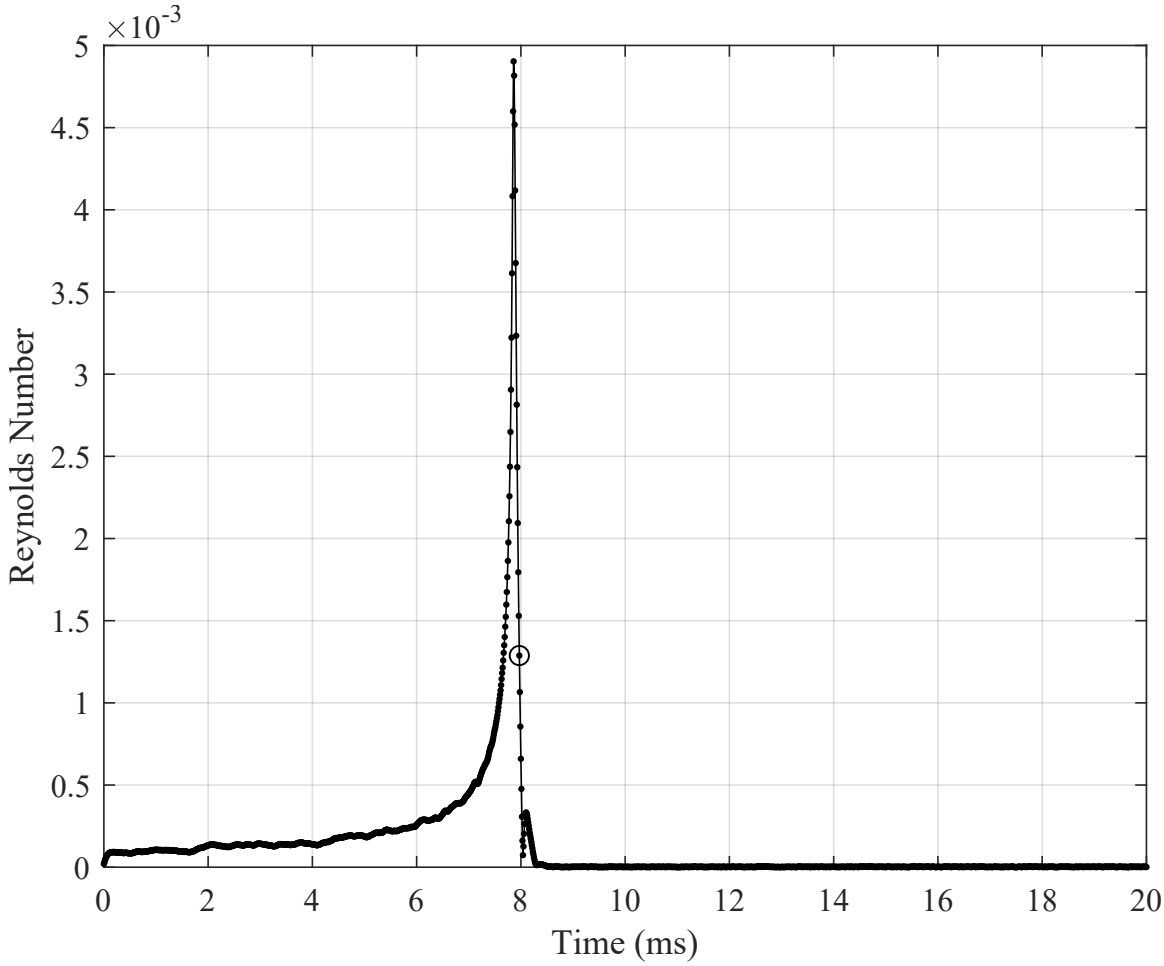

Figure 5.5: Raynolds number versus time for 990nm bead (the marker ◯ indicate the first closest approach (FCA) to the focal point)

ance of overdamped motion. These are the same conclusions drawn in [39] for the nearly overdamped motion of the micron-sized objects observed. Overdamped motion was also observed in the optical trapping of micron-sized beads in [34]. In contrast, a large Reynolds number implies that the inertial forces have a much larger effect on the bead's motion than the viscous forces. In other words, the effects of momentum are much more important than those of viscosity, which yields underdamped motion. However, the simulation data presented in figures 5.1 and 5.2 do not align with the characteristics associated with a low Reynolds number.

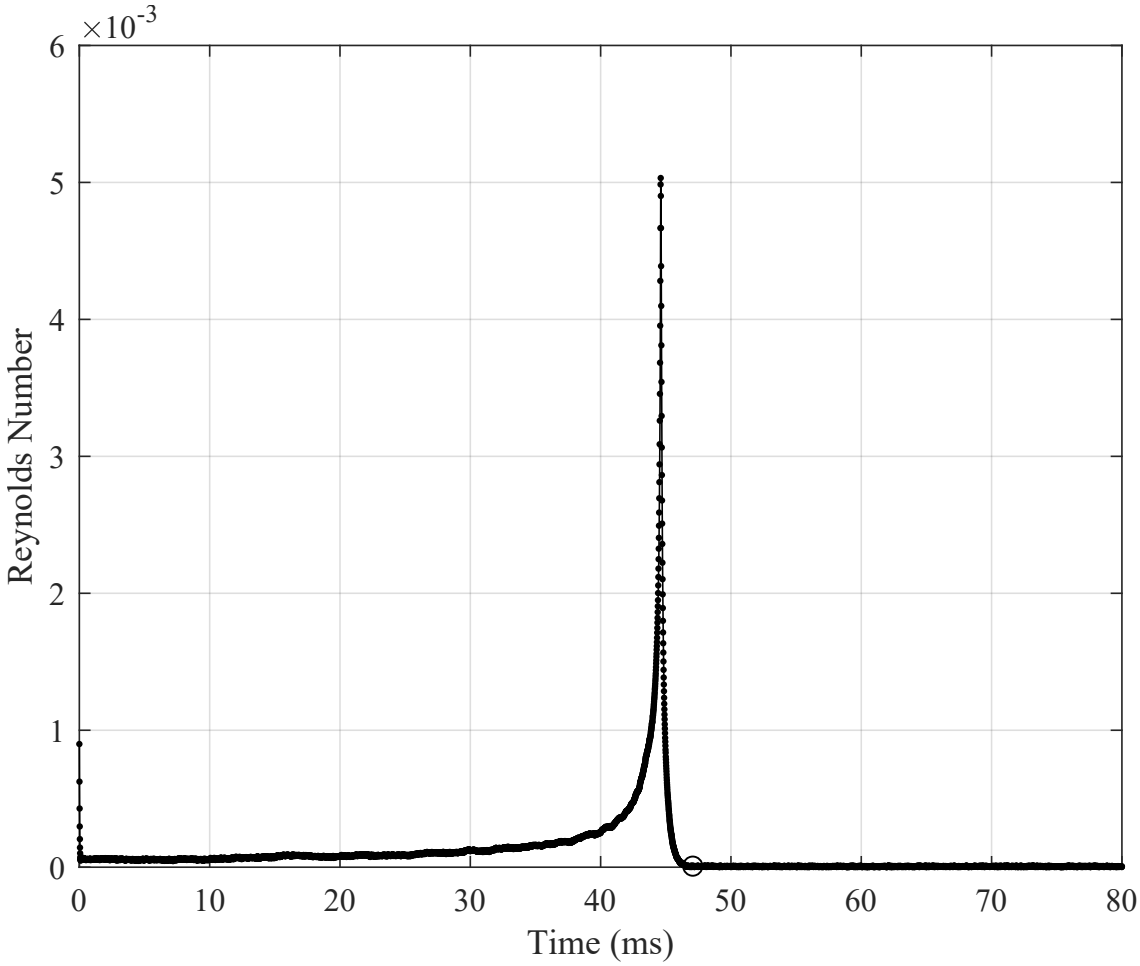

Figure 5.6: Raynolds number versus time for 1950nm bead (the marker ◯ indicate the first closest approach (FCA) to the focal point)

It can be observed from the figures 5.4 through 5.6 that the Reynolds number for all three cases is very small, $Re \leq 10^{-4}$, throughout the simulation except near the focal point. Moreover, it can be observed that the Reynolds number, during the bead's first closest approach to the focal point, becomes smaller as the bead's diameter increases. Large translational velocity at the first closest approach is the reason for large Reynolds number as it is directly proportional to the relative velocity of the bead and surrounding fluid. This can be observed in the figures 5.7 through 5.9. Moreover, this large relative velocity is the effect of retaining mass properties in

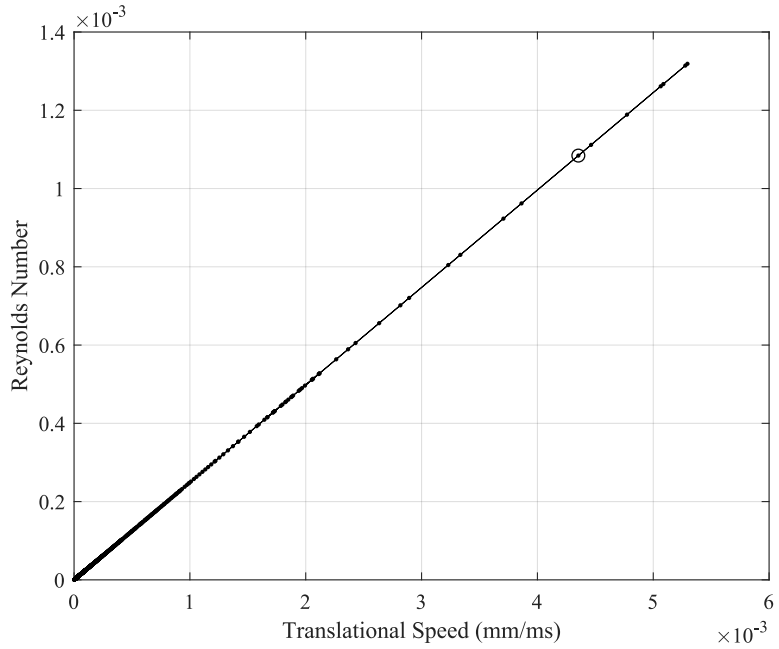

Figure 5.7: Raynolds number versus translational velocity for 500nm bead (the marker ◯ indicate the first closest approach (FCA) to the focal point)

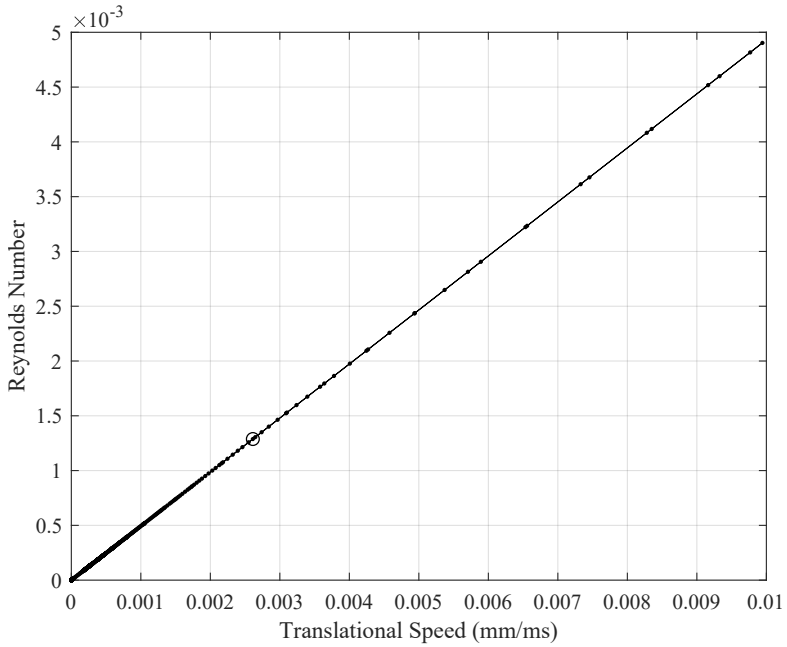

Figure 5.8: Raynolds number versus translational velocity for 990nm bead (the marker ◯ indicate the first closest approach (FCA) to the focal point)

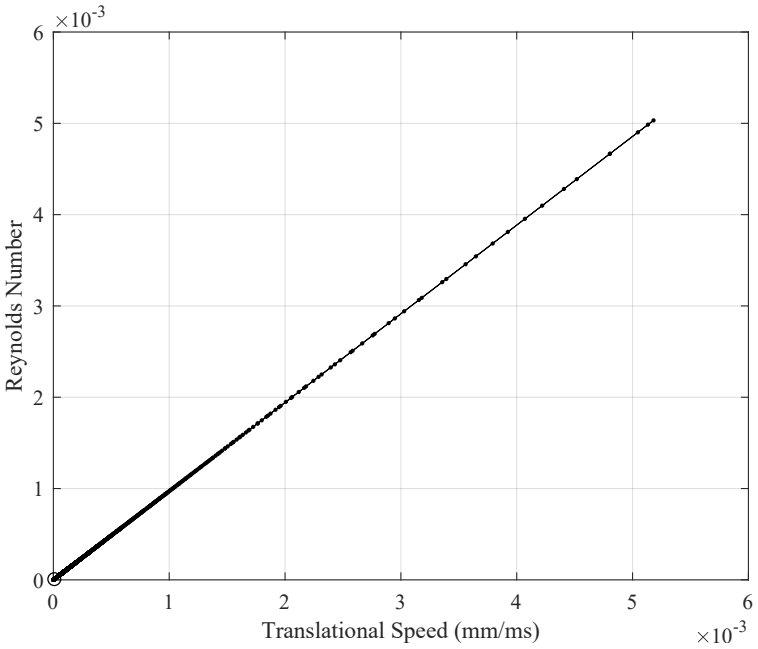

Figure 5.9: Raynolds number versus translational velocity for 1950nm bead (the marker ◯ indicate the first closest approach (FCA) to the focal point)

the bead's equations of motion which is completely opposite to the assumption made to develop the overdamped Langevin equations.

Neglecting mass and inertia properties of the bead in overdamped Langevin equations make the forces and moments directly define the velocity of the bead. This is evident from the equation given below which is derived by neglecting the mass matrix being zero in equation 4.4.

$$\dot{\mathbf{q}} = \frac{1}{\beta}\left(D^{-1}\mathbf{\Gamma}_{others}\left(\mathbf{q}, t\right)\right) \tag{5.2}$$

To the contrary, when the mass and inertia properties are retained, the forces and moments determine acceleration. Furthermore, when the motion forces and motion moments cancel each other at an equilibrium, are equal to zero, the velocity of the bead should also be equal to zero according to the overdamped Langevin equations. This gives a mathematical prediction of overdamped motion that should closely ap-

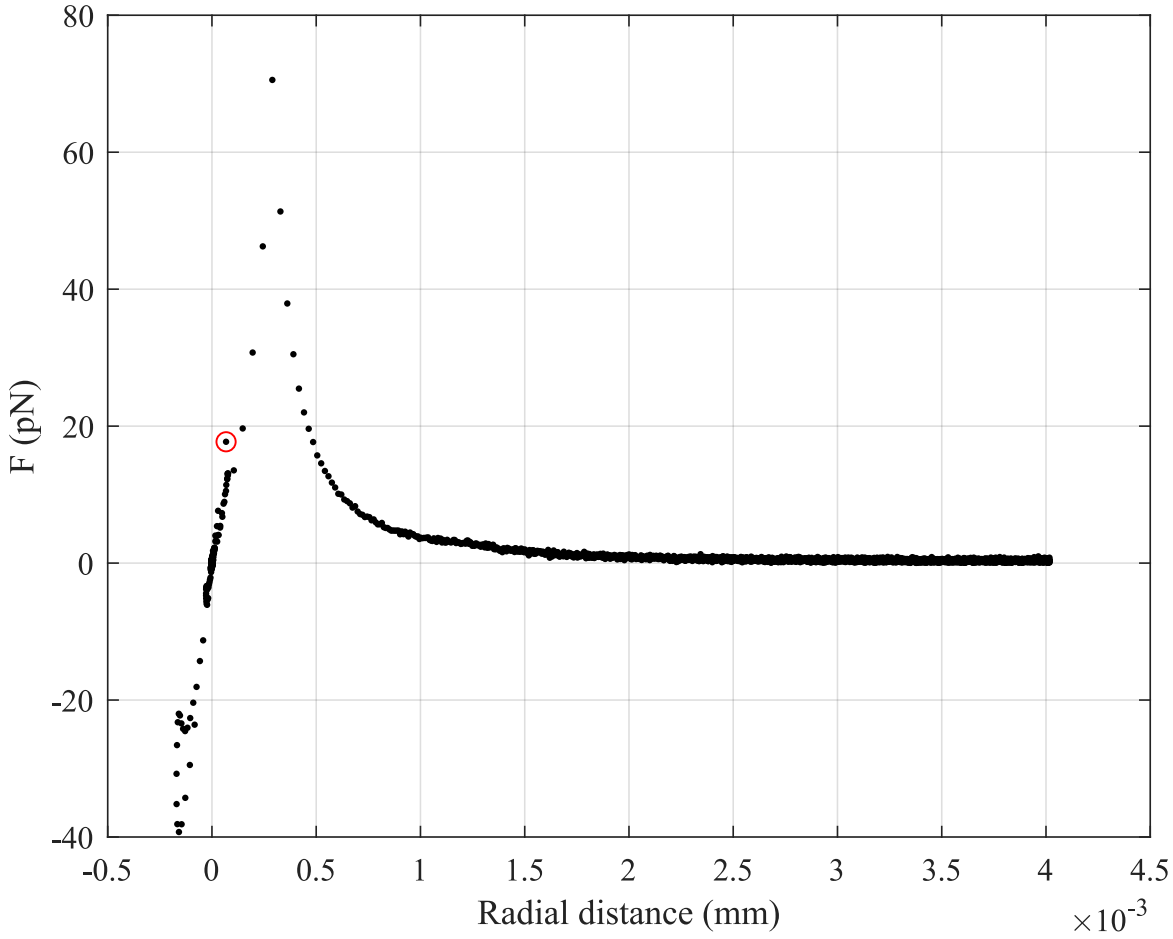

Figure 5.10: Net motion force versus radial distance for 500nm Bead (the marker ◯ indicate the first closest approach (FCA) to the focal point)

proximate the nearly overdamped actual motion of a micron-sized bead in the optical trap.

In the case of optical tweezers, the focal line of the optical trap happens to be a set of marginally stable equilibria, so the net motion force should approach zero within a small neighborhood of the focal point. Figures 5.10 through 5.12 investigate whether this is correct for the beam model used in this work. All three figures show that the net motion force approaches zero at the focal point, which is chosen as the origin of each plot. The negative forces indicate when the bead is above the focal

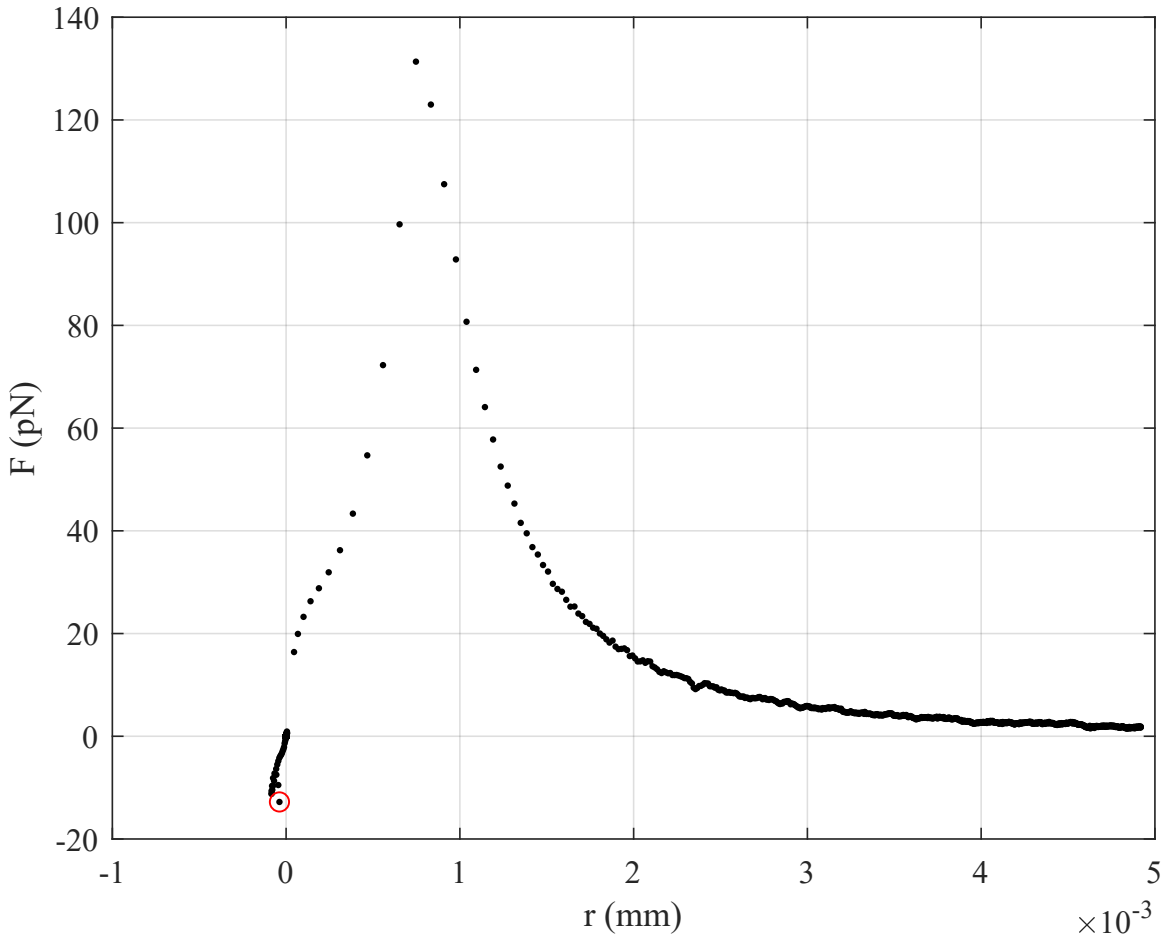

Figure 5.11: Net motion force versus radial distance for 990nm Bead (the marker ◯ indicate the first closest approach (FCA) to the focal point)

point, and the positive forces indicate when the bead is below the focal point. Notice that the peak of the motion force moves closer to the focal point as the diameter of the beads decreases. Also notice that the forces associated with Brownian motion create the jagged tail of the force profile shown in figures 5.10 through 5.12. This is because the random forces associated with Brownian motion become more dominant as the size of the motion forces decreases far from the focal point. This also occurs near the focal point and results in the 'ringing' or small flucuations in position that occur after the bead settles into a small region around the focal point.

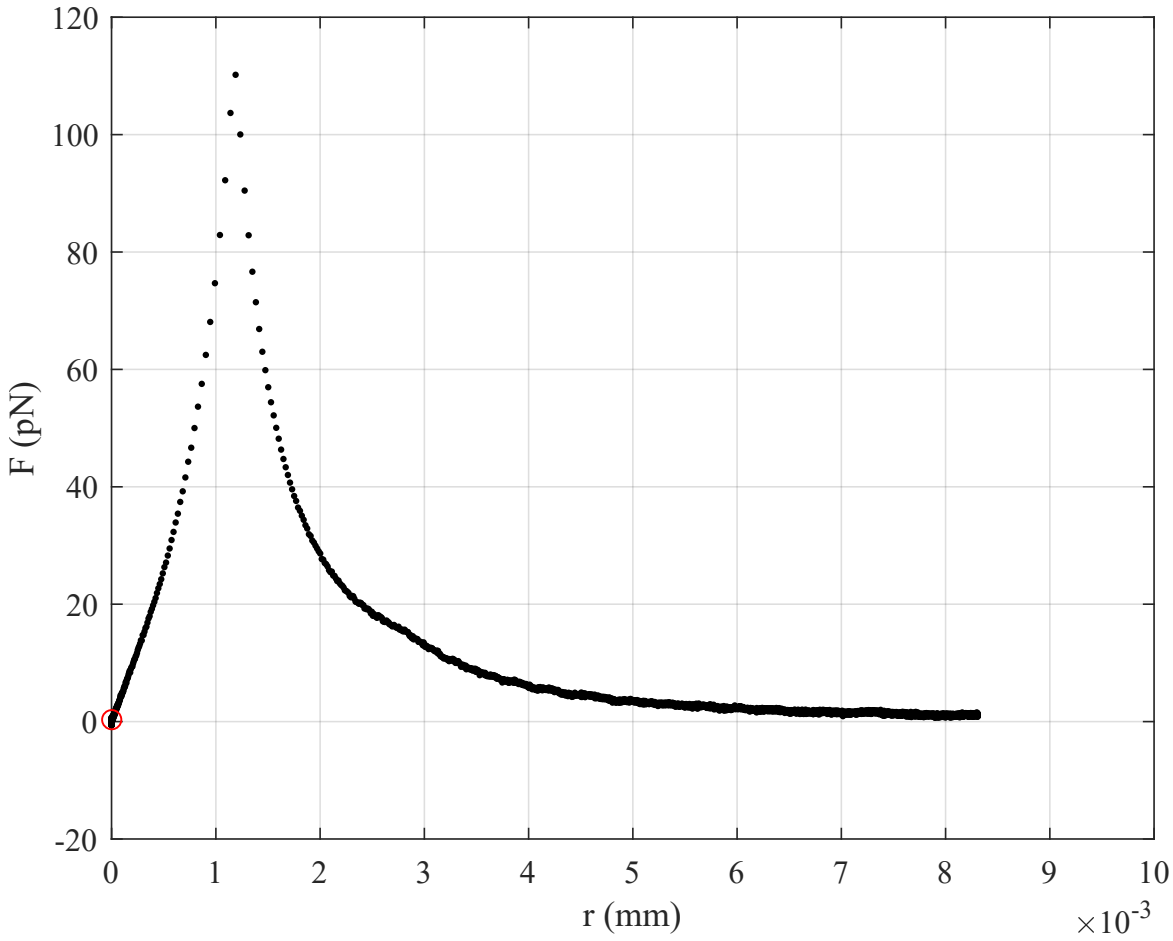

Figure 5.12: Net motion force versus radial distance for 1950nm Bead (the marker ◯ indicate the first closest approach (FCA) to the focal point)

As discussed in the previous paragraph, the net motion force approach zero within a small neighborhood of the focal point. Thus, if the bead is not close to the focal point, the integration of a first order model (the overdamped Langevin equations) enforces the assumption that the bead always moves at its terminal velocity, culminating in an overdamped approach to the equilibrium. Figures 5.13 through 5.15 show a comparison of the actual velocity and the terminal velocity calculated using equation (5.2).

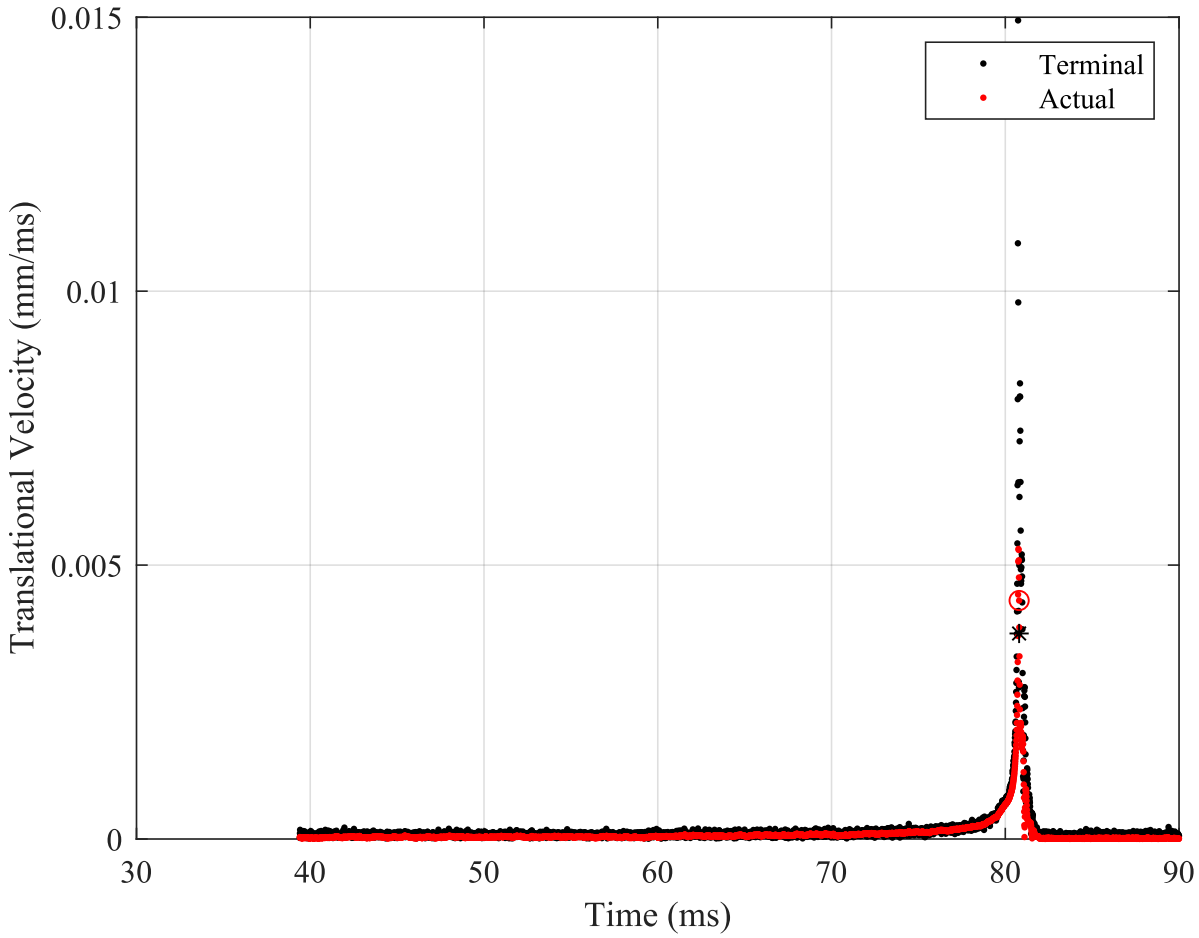

Figure 5.13: Terminal and actual translational speed over time for 500nm Bead (markers ◯ and ∗ indicate the first closest approach (FCA) to the focal point for actual and terminal velocity respectively)

The first thing to notice is that in figure 5.15, the actual velocity predicted by the bead model presented here aligns closely with the terminal speed predicted by the overdamped Langevin equations. In fact, the speeds predicted at first approach to the focal point are nearly identical. This explains why the 1950nm bead's motion aligns so closely with the predictions of the Reynolds number. Examination of figure 5.14 for the 990nm bead shows a small departure of the actual speeds from the terminal speeds. Although it appears that the terminal speed is greater than the actual speed, at the first nearest approach to the focal point, the actual speed is in general greater

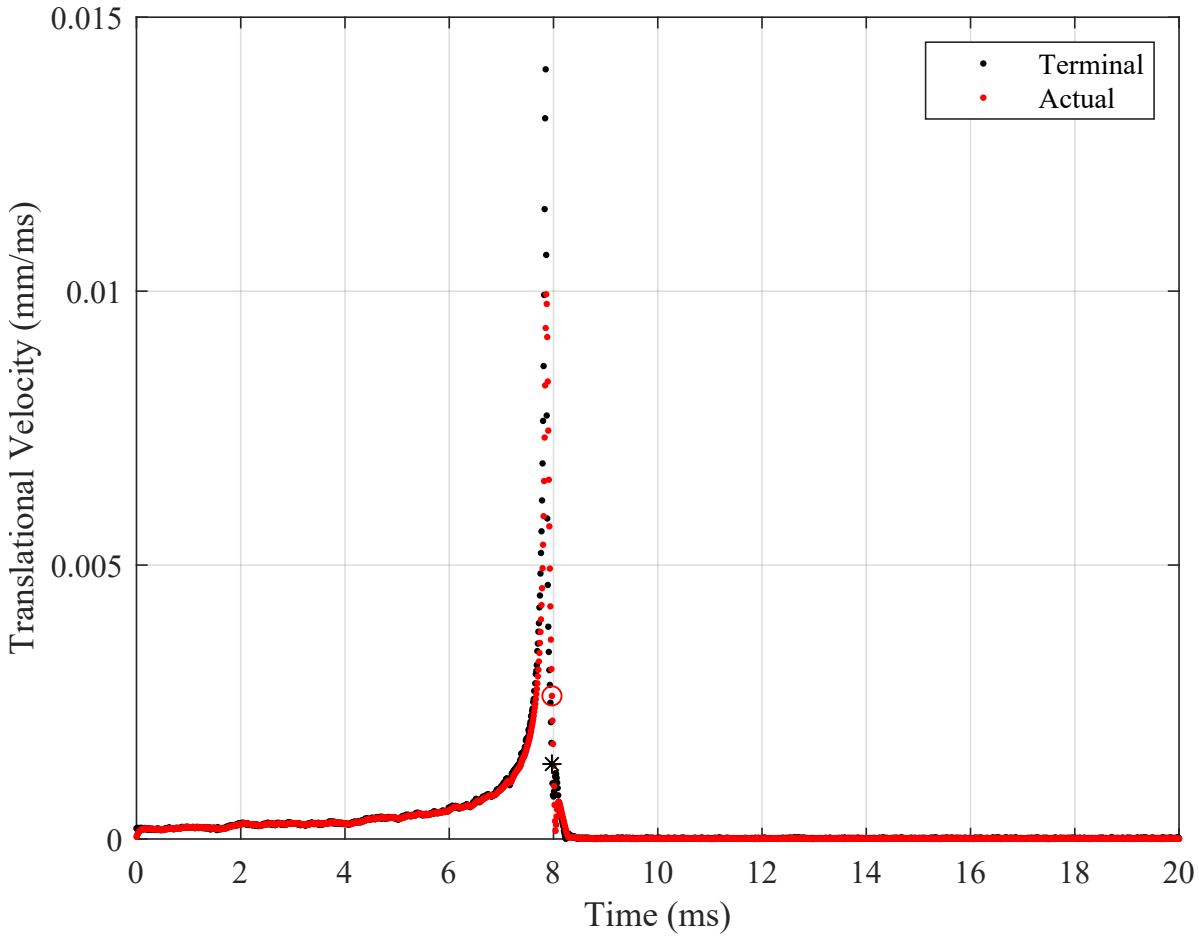

Figure 5.14: Terminal and actual translational speed over time for 990nm Bead (markers ◯ and ∗ indicate the first closest approach (FCA) to the focal point for actual and terminal velocity respectively)

than the terminal speed. This can occur because of the effects of momentum on the 990nm bead, which is not accounted for in the calculation of the terminal speed in the equation (5.2). Thus, it is not likely that the Reynolds number would predict the dynamic behavior of the 990nm. This conclusion is more evident for the 500nm bead in figure 5.13. The actual speeds deviate much farther from the terminal speeds even though the terminal speed appear to be larger than the actual ones at the first closest approach to the focal point. Again, this is because of the effect of momentum that is lost in equation (5.2). Figure 5.13 shows that the overdamped Langevin equations

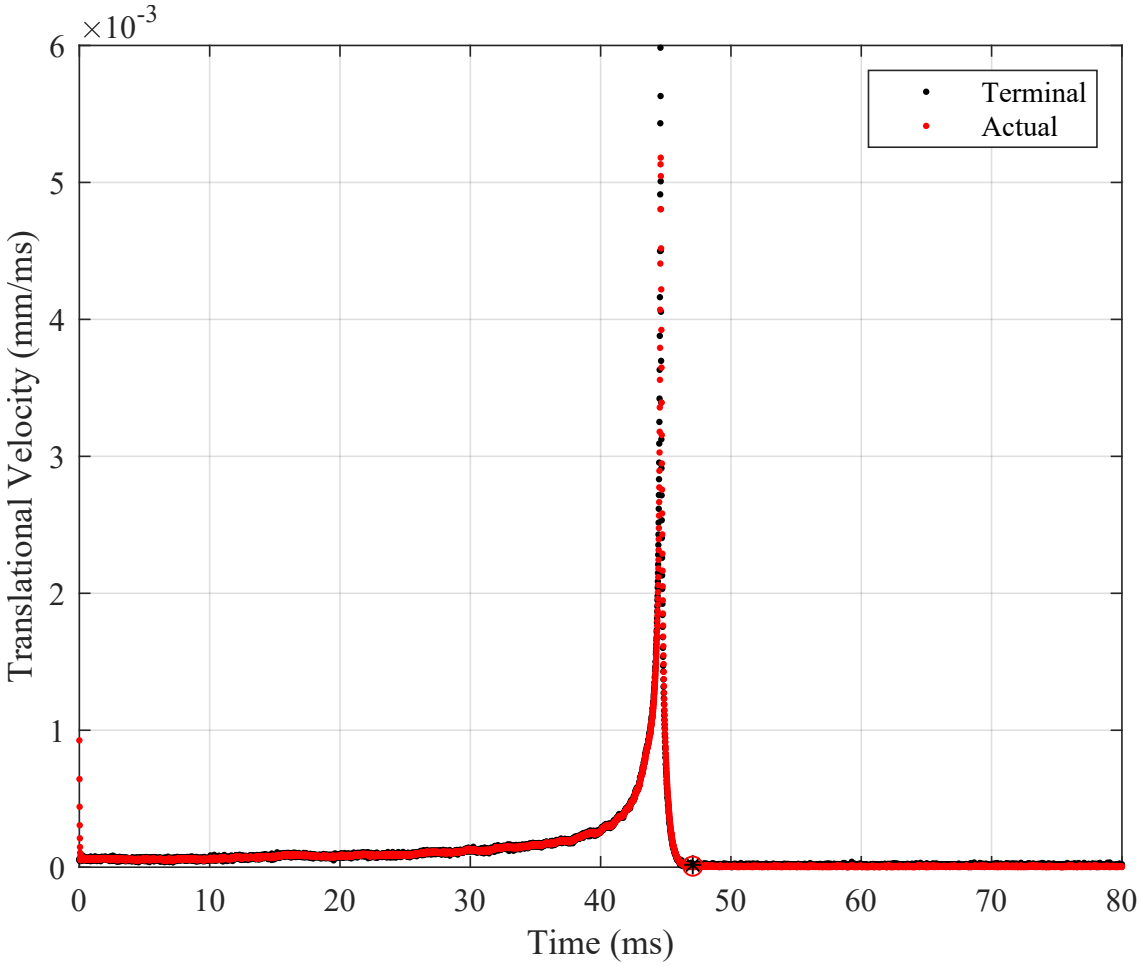

Figure 5.15: Terminal and actual translational speed over time for 1950nm Bead (markers ◯ and ∗ indicate the first closest approach (FCA) to the focal point for actual and terminal velocity respectively)

simply do not predict the motion of this smaller bead and therefore the Reynolds number cannot predict its motion.

CHAPTER 6

CONCLUSION AND FUTURE WORK

This work presented a three dimensional model to simulate the motion of a microbead under the influence of optical forces in an optical trap. Multiple scale analysis was used to deal with the discrepancies between inertia and drag forces in the equations of motion. This thesis also showed how a drawback in the motion capture technology, the inability to measure the motion in $\widehat{\mathbf{N}}_3$ direction, can be overcome using modeling and simulation to fill in the immeasurable data. This allowed the further analysis of the dynamics of microbead.

The simulation data provided velocity and acceleration information which allowed examination of the instantaneous Reynolds number. The computed values of Reynolds number for all three cases of 500nm, 990nm and 1950nm beads suggested that their motion will always be overdamped. Though the prediction from Reynolds number held true for 1950nm bead, underdamped motion was observed near the focal point for the cases of 500nm and 990nm beads. This concludes that the Reynolds number does not appear to have any value in predicting the behavior of objects of a size smaller than one micron.

The question still remains is that why the predictions of the Reynolds number do not hold true below the length scale of one micron. There is not much difference between the Reynolds number of the different beads. The data available from experiments do provide much information. Simulations allowed a detailed analysis of the bead's motion and the forces acting on it. However, this simulation model can be improved further to get the results closer to the reality. Stokes' law is used here to

compute drag forces acting on the microbead. However, the Stokes' law assumes that the fluid flow around the particle is in steady state. Which is not the case here as the bead's acceleration is not zero. Maxey-Riley equation of motion for a sphere[32] can be used here to account for all the fluid forces acting on the bead.

Another area where this model can be improved is the calculation of optical forces. The approach of geometric ray-optics is used here to discretize the laser beam into a number of rays moving in a straight line. However, this approach is less accurate when the particle size is in the order of laser's wavelength as discussed in Chapter 3. However being computationally more expensive, the generalized lorenz-mie theory (GLMT)[18] can be used here to compute more accurate force values.

Finally, It is also desirable to perform more experiments using an optical tweezer that can provide more accurate measurements of the bead's position and the forces applied to the bead. These improvements will be pursued in the future work.

APPENDIX A

EULER PARAMETERS

To simulate a sphere freely spinning in three dimensions, euler parameters can be used to avoid any kind of singularity in the rotation matrix. One of the major issue here is the enforcement of normality constraint on the euler parameters. State of the art is an elaborate constraint embedding technique[24]. This appendix discusses another simpler way to do constraint embedding for euler parameters. The writing format used below is adapted from [9].

Rigid Bodies: There is one rigid body, the sphere.

Inertial Reference Frame and Point: The inertial reference point is N, and N $= \left(\widehat{\mathbf{N}}_1, \widehat{\mathbf{N}}_2, \widehat{\mathbf{N}}_3\right)$ is the inertial reference frame.

Other Points and Frames: Point A is body-attached point and it is also the center of gravity of body, and A $= \left(\widehat{\mathbf{A}}_1, \widehat{\mathbf{A}}_2, \widehat{\mathbf{A}}_3\right)$ is body-attached frame.

Location Descriptions: It is difficult to discern a physical meaning for each Euler parameter. So, only rotation matrix is given here which represents sphere's orientation.

$$L_A = \left\{\mathbf{P}_{\mathrm{NA}},\ {}^N_A R\right\} + geom. \qquad \mathbf{P}_{\mathrm{NA}} = q_1\widehat{\mathbf{N}}_1 + q_2\widehat{\mathbf{N}}_2 + q_3\widehat{\mathbf{N}}_3 \tag{A.1}$$

$${}^N_A R = \frac{1}{e_0^2+e_1^2+e_2^2+e_3^2}\begin{bmatrix} e_0^2+e_1^2-e_2^2-e_3^2 & 2\left(e_1e_2-e_0e_3\right) & 2\left(e_1e_3+e_0e_2\right) \\ 2\left(e_1e_2+e_0e_3\right) & e_0^2-e_1^2+e_2^2-e_3^2 & 2\left(e_2e_3-e_0e_1\right) \\ 2\left(e_1e_3-e_0e_2\right) & 2\left(e_2e_3+e_0e_1\right) & e_0^2-e_1^2-e_2^2+e_3^2 \end{bmatrix} \tag{A.2}$$

Coordinates: Seven coordinates appear in the location descriptions. Where, q_1 through q_3 are translational coordinates representing sphere's position and e_0 through e_3 (Euler parameters) are rotational coordinates representing sphere's orientation. Also,

$$\mathbf{q} = \begin{bmatrix} q_1 & q_2 & q_3 \end{bmatrix}^{\mathrm{T}} \qquad\qquad \mathbf{e} = \begin{bmatrix} e_0 & e_1 & e_2 & e_3 \end{bmatrix}^{\mathrm{T}} \tag{A.3}$$

Constraints: It is known that rotations only have three independent coordinates so there must be a single constraint that can be used to eliminate the forth rotational coordinate. It is the normalization constraint given as

$$e_0^2 + e_1^2 + e_2^2 + e_3^2 = 1 \tag{A.4}$$

Degrees of Freedom (DOFs):

$$7 \text{ coordinates - } 1 \text{ constraint} = 6 \text{ DOFs}$$

Objectives: Find equations of motion.

Velocity: The translational velocity of the mass center A is

$$\mathbf{V}_{\mathrm{A}} = \frac{d\mathbf{P}_{\mathrm{NA}}}{dt} = \dot{q}_1 \widehat{\mathbf{N}}_1 + \dot{q}_2 \widehat{\mathbf{N}}_2 + \dot{q}_3 \widehat{\mathbf{N}}_3 \tag{A.5}$$

The angular velocity of body A is

$$\begin{aligned} {}^{\mathrm{N}}\omega^{\mathrm{A}} = {} & 2\left(e_0\dot{e}_1 - e_1\dot{e}_0 - e_2\dot{e}_3 + e_3\dot{e}_2\right)\widehat{\mathbf{A}}_1 + 2\left(e_0\dot{e}_2 + e_1\dot{e}_3 - e_2\dot{e}_0 - e_3\dot{e}_1\right)\widehat{\mathbf{A}}_2 \\ & + 2\left(e_0\dot{e}_3 - e_1\dot{e}_2 + e_2\dot{e}_1 - e_3\dot{e}_0\right)\widehat{\mathbf{A}}_3 \end{aligned} \tag{A.6}$$

$$\therefore \ {}^{\mathrm{N}}\omega^{\mathrm{A}} = 2 \underbrace{\begin{bmatrix} -e_1 & e_0 & e_3 & -e_2 \\ -e_2 & -e_3 & e_0 & e_1 \\ -e_3 & e_2 & -e_1 & e_0 \end{bmatrix}}_{L} \underbrace{\begin{bmatrix} \dot{e}_0 \\ \dot{e}_1 \\ \dot{e}_2 \\ \dot{e}_3 \end{bmatrix}}_{\dot{\mathbf{e}}} = L\dot{\mathbf{e}} \tag{A.7}$$

Note: The angular velocity is represented in body-attached frame.

Acceleration: The translational acceleration of mass center A is

$$\dot{\mathbf{V}}_{\mathrm{A}} = \frac{d\mathbf{V}_{\mathrm{A}}}{dt} = \ddot{q}_1 \widehat{\mathbf{N}}_1 + \ddot{q}_2 \widehat{\mathbf{N}}_2 + \ddot{q}_3 \widehat{\mathbf{N}}_3 \tag{A.8}$$

The angular acceleration of body A is

$${}^{\mathrm{N}}\dot{\omega}^{\mathrm{A}} = \frac{d^{\mathrm{N}}\omega^{\mathrm{A}}}{dt} = \dot{L}\dot{\mathbf{e}} + L\ddot{\mathbf{e}} \tag{A.9}$$

where,

$$\dot{L} = 2\begin{bmatrix} -\dot{e}_1 & \dot{e}_0 & \dot{e}_3 & -\dot{e}_2 \\ -\dot{e}_2 & -\dot{e}_3 & \dot{e}_0 & \dot{e}_1 \\ -\dot{e}_3 & \dot{e}_2 & -\dot{e}_1 & \dot{e}_0 \end{bmatrix}, \qquad \ddot{\mathbf{e}} = \begin{bmatrix} \ddot{e}_0 \\ \ddot{e}_1 \\ \ddot{e}_2 \\ \ddot{e}_3 \end{bmatrix}$$

Note: The angular acceleration is represented in body-attached frame.

Mass Properties: Mass of body A is assumed to be m_{A}. The inertia matrix of body A can be given as

$$I_{\mathrm{AA}} = \begin{bmatrix} I_{11} & 0 & 0 \\ 0 & I_{22} & 0 \\ 0 & 0 & I_{33} \end{bmatrix}$$

Forces and Moments: Here it is assumed that the sum of all external forces **F** acting on the body is known and is represented in inertial frame. And, sum of all the moments **M** acting about center of gravity of the body is known and is represented in body-attached frame.

Equations of Motion: Here, Euler's laws of motion will be used to calculate the equations of motion. As per Euler's first law of motion, the sum of external forces is equal to the inertia force of the body. Therefore,

$$m_{\mathrm{A}}\dot{\mathbf{V}}_{\mathrm{A}} = \mathbf{F} \tag{A.10}$$

$$\therefore m_{\mathrm{A}} \begin{bmatrix} \ddot{q}_1 \\ \ddot{q}_2 \\ \ddot{q}_3 \end{bmatrix} = \begin{bmatrix} F_{N_1} \\ F_{N_2} \\ F_{N_3} \end{bmatrix} \tag{A.11}$$

$$\therefore \underbrace{\begin{bmatrix} m_{\mathrm{A}} & 0 & 0 \\ 0 & m_{\mathrm{A}} & 0 \\ 0 & 0 & m_{\mathrm{A}} \end{bmatrix}}_{A_{(3\times3)}} \underbrace{\begin{bmatrix} \ddot{q}_1 \\ \ddot{q}_2 \\ \ddot{q}_3 \end{bmatrix}}_{\ddot{\mathbf{q}}_{(3\times1)}} = \underbrace{\begin{bmatrix} F_{N_1} \\ F_{N_2} \\ F_{N_3} \end{bmatrix}}_{\mathbf{F}_{(3\times1)}} \tag{A.12}$$

As per Euler's second law of motion, the rate of change of angular momentum about body's center of gravity is equal to the sum of external moments acting on the body about the same point. Therefore,

$$\frac{d\mathbf{H}_{\mathrm{AA}}}{dt} = \mathbf{M} \tag{A.13}$$

where,

$$\frac{d\mathbf{H}_{\mathrm{AA}}}{dt} = \dot{\mathbf{H}}_{\mathrm{AA}} = I_{\mathrm{AA}}{}^{\mathrm{N}}\dot{\omega}^{\mathrm{A}} + {}^{\mathrm{N}}\omega^{\mathrm{A}} \times \left(I_{\mathrm{AA}}{}^{\mathrm{N}}\omega^{\mathrm{A}}\right) \tag{A.14}$$

Substituting values from equations (A.7) and (A.9), we get

$$\dot{\mathbf{H}}_{\mathrm{AA}} = I_{\mathrm{AA}}\left(\dot{L}\dot{\mathbf{e}} + L\ddot{\mathbf{e}}\right) + (L\dot{\mathbf{e}}) \times (I_{\mathrm{AA}}(L\dot{\mathbf{e}})) \tag{A.15}$$

$$\therefore \dot{\mathbf{H}}_{\mathrm{AA}} = I_{\mathrm{AA}}L\ddot{\mathbf{e}} + I_{\mathrm{AA}}\dot{L}\dot{\mathbf{e}} + (L\dot{\mathbf{e}}) \times (I_{\mathrm{AA}}L\dot{\mathbf{e}}) \tag{A.16}$$

For convenience, an intermediate variable $\mathbf{K}$ can be defined as

$$\mathbf{K} = I_{\mathrm{AA}}\dot{L}\dot{\mathbf{e}} + (L\dot{\mathbf{e}}) \times (I_{\mathrm{AA}}L\dot{\mathbf{e}}) \tag{A.17}$$

So,

$$\dot{\mathbf{H}}_{\mathrm{AA}} = I_{\mathrm{AA}}L\ddot{\mathbf{e}} + \mathbf{K} \tag{A.18}$$

It can be observed from the equation above that the dimensions of matrix L is 3×4 and that of vector K is 3×1. Substituting equation (A.18) in equation (A.13), we get

$$I_{\mathrm{AA}}L\ddot{\mathbf{e}} + K = \mathbf{M} \tag{A.19}$$

$$\therefore I_{\mathrm{AA}}L\ddot{\mathbf{e}} = \mathbf{M} - \mathbf{K} \tag{A.20}$$

It is important to keep in mind that equation (A.20) is in body-attached frame. It can be observed here that $I_{\mathrm{AA}}L$ will result in a 3×4 matrix. Also, the right hand side of equation (A.20) is a 3×1 vector. Equation (A.12) represents the translational equations of motion. It can be observed that the number of unknowns (Translational accelerations) is exactly equal to number of equations. And so, system can be easily solved if there was no rotation. But, equation (A.20) which represents rotational equations of motion, has less number of equations than the unknowns (Euler accelerations). So, there is a need of one more equation (a constraint) to solve this system. The normality constraint for euler parameters can be used here. Representing equation (A.4) in the vector form

$$\mathbf{e}^{\mathrm{T}}\mathbf{e} = 1 \tag{A.21}$$

Differentiating this equation

$$\mathbf{e}^{\mathrm{T}}\dot{\mathbf{e}} = 0 \tag{A.22}$$

Differentiating again

$$\mathbf{e}^{\mathrm{T}}\ddot{\mathbf{e}} = -\dot{\mathbf{e}}^{\mathrm{T}}\dot{\mathbf{e}} \tag{A.23}$$

Here, equations (A.21), (A.22) and (A.23) are position, velocity and acceleration level constraints respectively. For Euler parameters to work properly, equation (A.23) has to be satisfied. So, equation (A.23) can be appended to equation (A.20). Thus the under-determined rotational equations of motion are now perfectly constrained.

$$\underbrace{\begin{bmatrix} I_{\mathrm{AA}}L \\ \mathbf{e}^{\mathrm{T}} \end{bmatrix}}_{\widetilde{I}_{(4\times4)}} \ddot{\mathbf{e}} = \underbrace{\begin{bmatrix} \mathbf{M} - \mathbf{K} \\ -\dot{\mathbf{e}}^{\mathrm{T}}\dot{\mathbf{e}} \end{bmatrix}}_{\widetilde{\mathbf{M}}_{(4\times1)}} \tag{A.24}$$

It can be observed that matrix $\widetilde{I}$ is never singular. Thus, the rotational equations of motion can be solved very easily now. So, all the equations of motion (equations (A.12) and (A.24)) can be combined as

$$\boxed{\begin{bmatrix} A_{(3\times3)} & 0_{(3\times4)} \\ 0_{(4\times3)} & \widetilde{I}_{(4\times4)} \end{bmatrix} \begin{bmatrix} \ddot{\mathbf{q}} \\ \ddot{\mathbf{e}} \end{bmatrix} = \begin{bmatrix} \mathbf{F}_{(3\times1)} \\ \widetilde{\mathbf{M}}_{(4\times1)} \end{bmatrix}} \tag{A.25}$$

Discussion: Though some assumptions were made here for inertia matrix, forces and moments, the calculation of rotational equation of motion is generic. So, this method can be applied to not only spherical particle but any kind of system where the use of Euler parameters is necessary.

Though equation (A.25) is analytically correct, one should be mindful while integrating it numerically. The acceleration level constraint (equation (A.23)) will be maintained very strongly. But, very small computational errors generated during solving equation (A.25) adds up quickly and then position and velocity level constraints (equation (A.21) and (A.22) respectively) will not be maintained anymore. So, to enforce position and velocity level constraints, the euler parameters has to be normalized and dependent euler speed has to be calculated each time before calculating euler accelerations. Assuming that e_0 is the dependent euler parameter, these calculations can be given as

$$\mathbf{e}_{\text{new}} = \frac{\mathbf{e}_{\text{old}}}{\|\mathbf{e}_{\text{old}}\|} , \qquad \dot{e}_0 = -\frac{1}{e_0}\left(e_1\dot{e}_1 + e_2\dot{e}_2 + e_3\dot{e}_3\right) \tag{A.26}$$

APPENDIX B

SIMULATION PARAMETERS

This appendix presents the simulation parameters used in the work presented in Chapters 2 through 4. Many of these parameters, such as the Density of different materials and Boltzmann constant, are well defined and readily available in research literature and textbooks.

Parameter	Description	Value	Unit
T	System temperature	293.15	k
k_b	Boltzmann constant	1.38×10^{-23}	$kg \cdot m/k^2 \cdot s$
g	Gravitational acceleration	9.80665	m/s^2
ρ_b	Density of bead's material	1050	kg/m^3
ρ_m	Density of fluid medium	998.2071	kg/m^3
μ_m	Dynamic viscosity of fluid medium	1.002×10^{-3}	$kg/m \cdot s$
n_P	Refractive index of the bead's material	1.57773	Unitless
n_m	Refractive index of fluid medium	1.33	Unitless
c	Speed of light in a vacuum	299792458	m/s
R_{obj}	Radius of objective lens	2.6×10^{-3}	m
NA	Numerical aperture of objective lens	1.3	Unitless
f	Focal length of objective lens	2×10^{-3}	m
λ	Wavelength of laser	0.8×10^{-6}	m
P_t	Total beam power	156×10^{-3}	$kg \cdot m^2/s^3$

Table B.1: Parameters common to all three cases

Table B.1 provides simulation parameters common to all three cases. While, tables B.2 through B.4 provides the simulation parameters specific to each case.

Parameter	Description	Value	Unit
r	Radius of the bead	0.25×10^{-6}	m
σ	Beam waist at objective lens	2.5×10^{-3}	m
a_2	Scaling factor	3×10^{-5}	Unitless

Table B.2: Parameters for the simulation of 500nm bead

Parameter	Description	Value	Unit
r	Radius of the bead	0.495×10^{-6}	m
σ	Beam waist at objective lens	1×10^{-3}	m
a_2	Scaling factor	1.2×10^{-3}	Unitless

Table B.3: Parameters for the simulation of 990nm bead

Parameter	Description	Value	Unit
r	Radius of the bead	0.975×10^{-6}	m
σ	Beam waist at objective lens	1.85×10^{-3}	m
a_2	Scaling factor	8×10^{-3}	Unitless

Table B.4: Parameters for the simulation of 1950nm bead

APPENDIX C

ADDITIONAL PLOTS

C.1 Change in total energy versus time

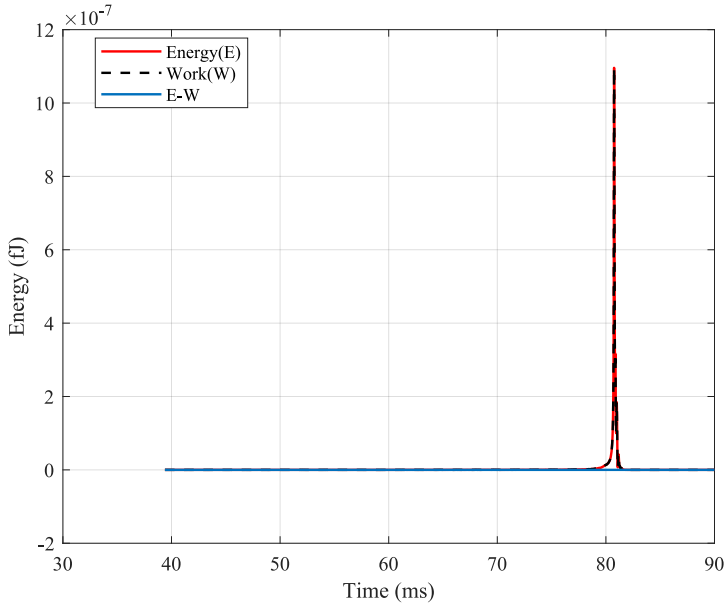

Figure C.1: 500nm bead

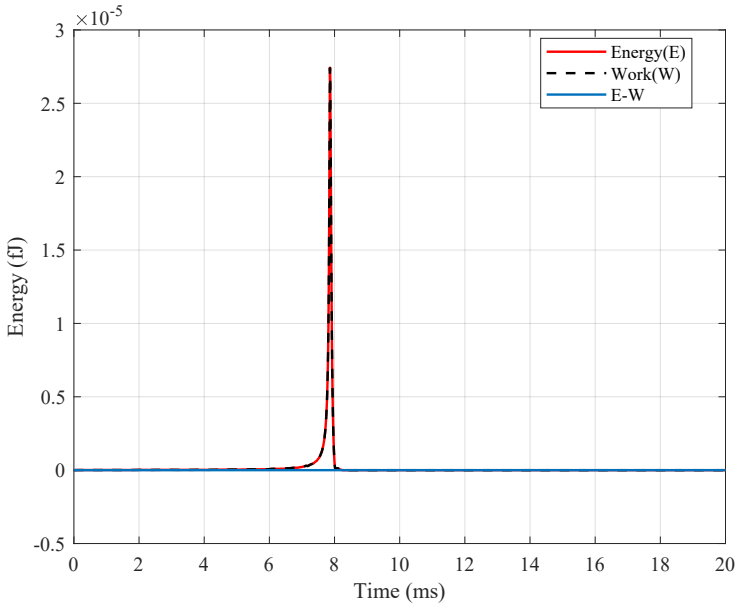

Figure C.2: 990nm bead

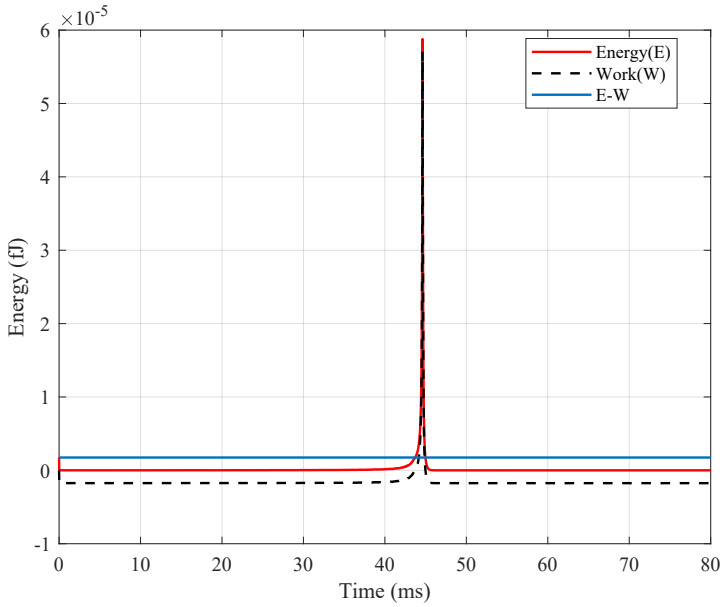

Figure C.3: 1950nm bead

C.2 Planer motion of the bead

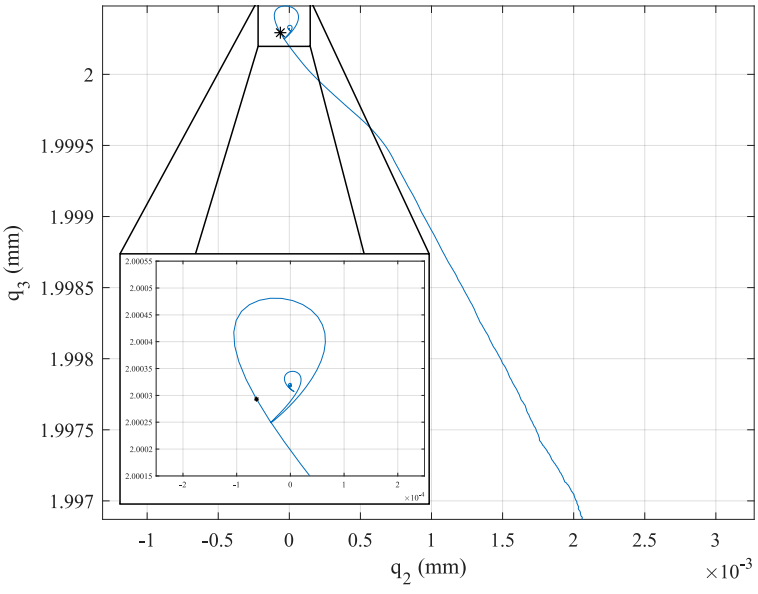

Figure C.4: 500nm bead

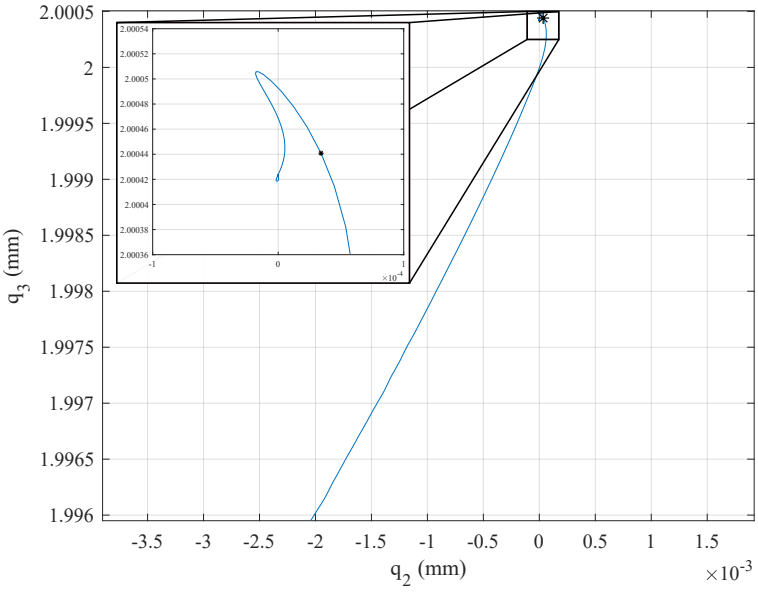

Figure C.5: 990nm bead

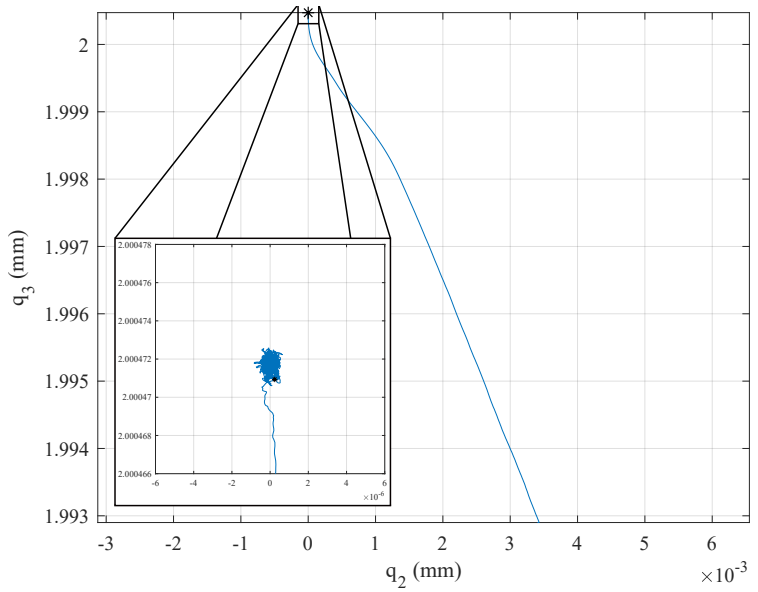

Figure C.6: 1950nm bead

C.3 Orientation of the bead versus time

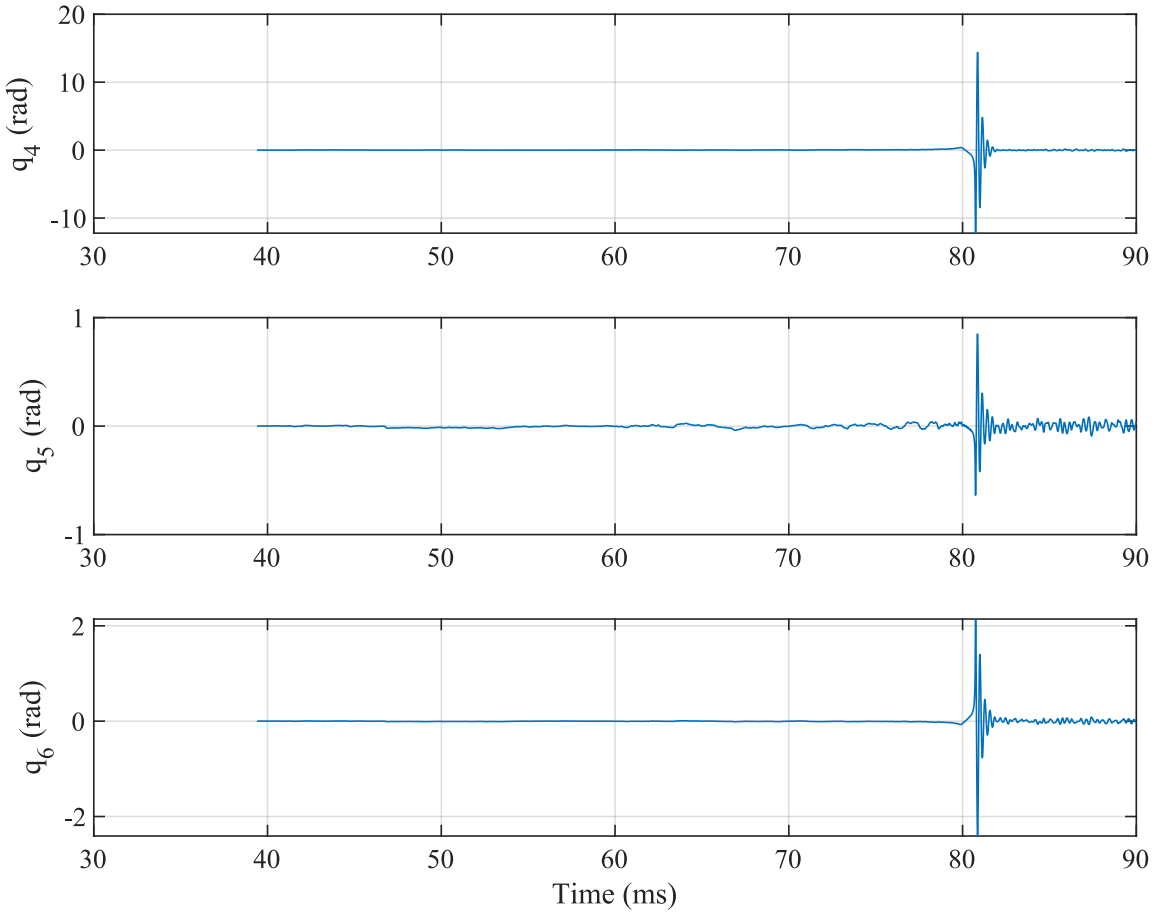

Figure C.7: 500nm bead

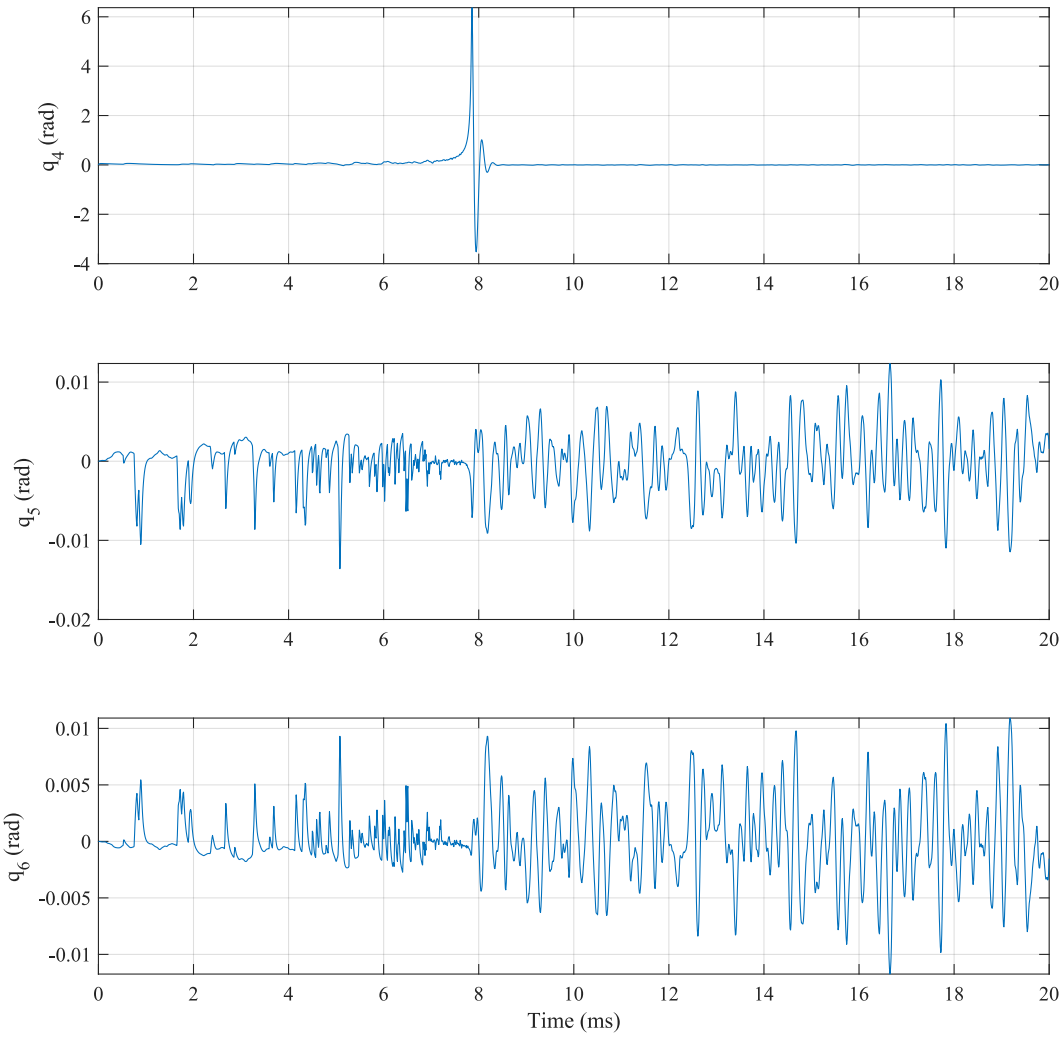

Figure C.8: 990nm bead

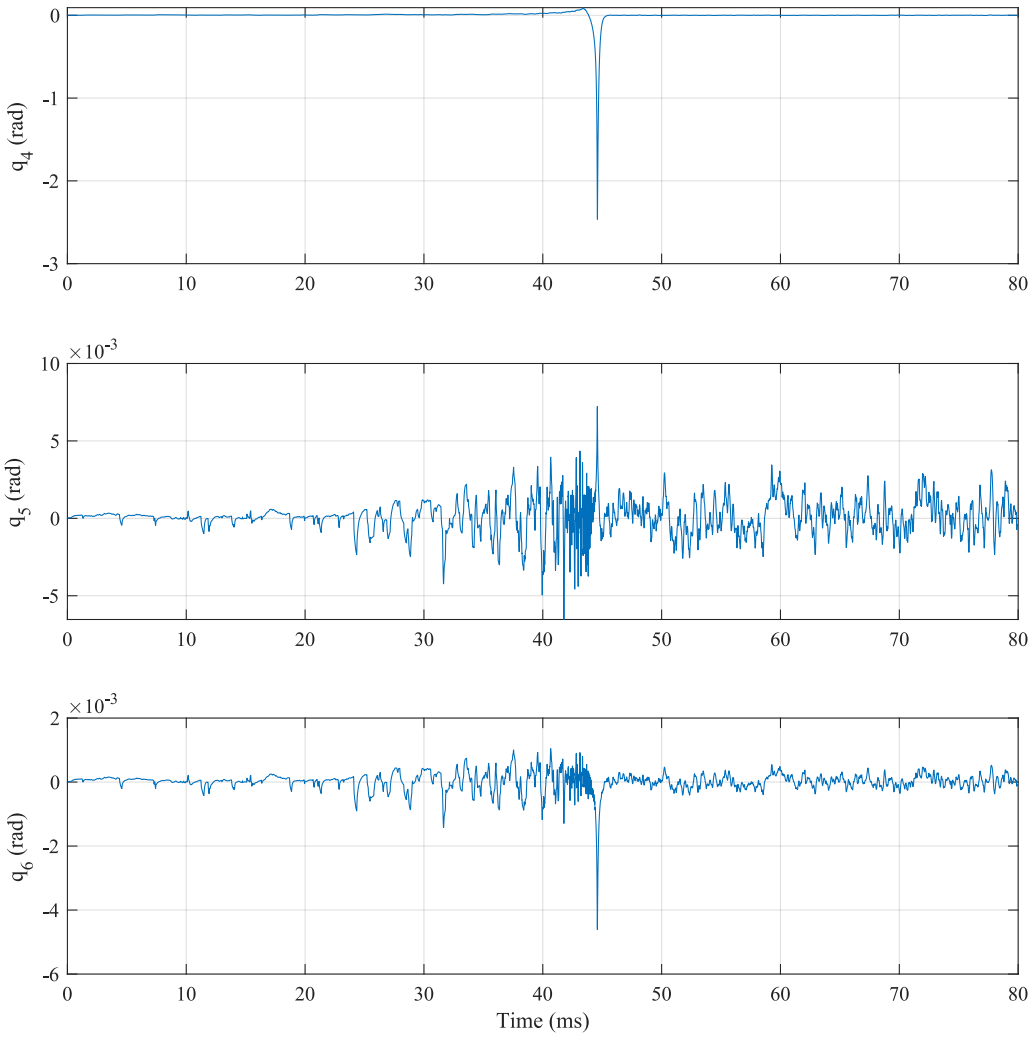

Figure C.9: 1950nm bead

C.4 Bead's motion $\widehat{\mathbf{N}}_3$ direction versus time

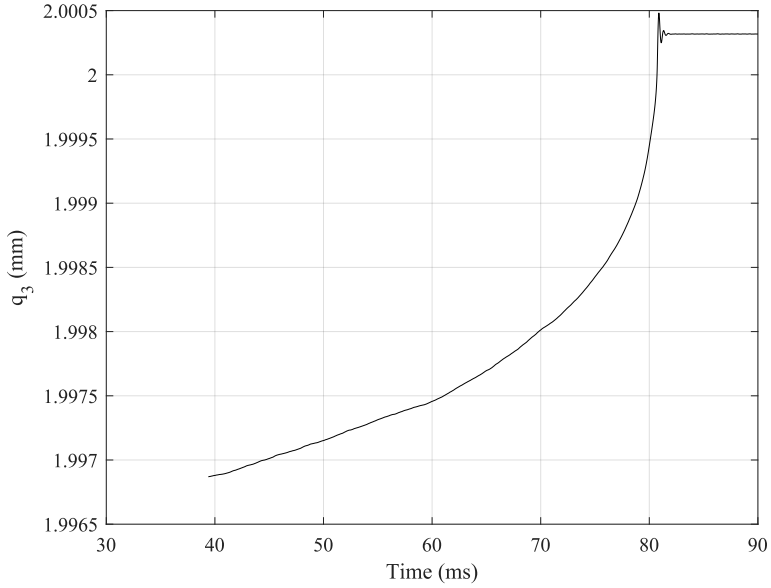

Figure C.10: 500nm bead

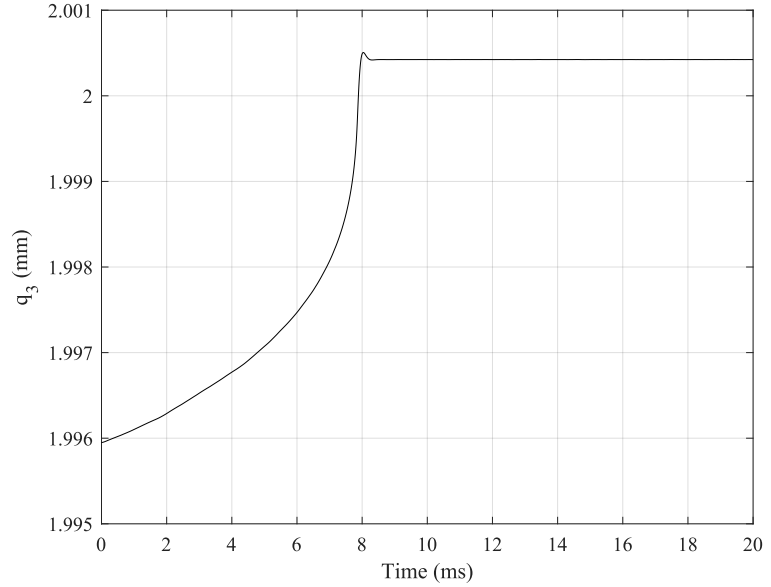

Figure C.11: 990nm bead

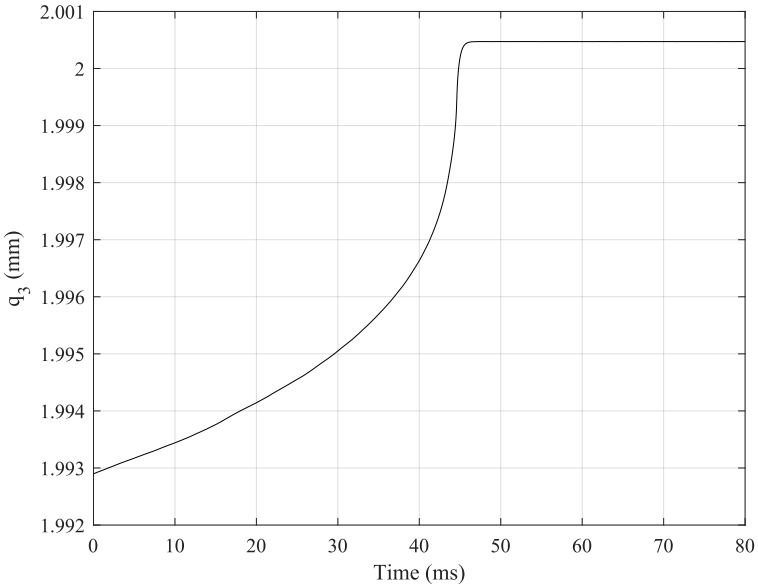

Figure C.12: 1950nm bead

REFERENCES

[1] Jonghoon Ahn et al. "Optically levitated nanodumbbell torsion Balance and GHz nanomechanical rotor". In: *Physical Review Letters* 121 (3 July 2018), p. 033603.

[2] A. Ashkin. "Acceleration and Trapping of Particles by Radiation Pressure". In: *Phys. Rev. Lett.* 24 (4 Jan. 1970), pp. 156–159.

[3] A. Ashkin. "Forces of a single-beam gradient laser trap on a dielectric sphere in the ray optics regime". In: *Biophysical Journal* 61.2 (1992), pp. 569–582. ISSN: 0006-3495.

[4] A. Ashkin. "Optical trapping and manipulation of neutral particles using lasers". In: *Proceedings of the National Academy of Sciences* 94.10 (1997), pp. 4853–4860. ISSN: 0027-8424.

[5] A. Ashkin. "History of optical trapping and manipulation of small-neutral particle, atoms, and molecules". In: *IEEE Journal of Selected Topics in Quantum Electronics* 6.6 (Nov. 2000), pp. 841–856.

[6] A. Ashkin and J. M. Dziedzic. "Optical Levitation by Radiation Pressure". In: *Applied Physics Letters* 19.8 (1971), pp. 283–285.

[7] A. Ashkin et al. "Observation of a single-beam gradient force optical trap for dielectric particles". In: *Opt. Lett.* 11.5 (May 1986), pp. 288–290.

[8] Johannes Berner et al. "Oscillating modes of driven colloids in overdamped systems". In: *Nature Communications* 9.1 (2018), p. 999.

[9] A. Bowling. *Vector Mechanics: A Systematic Approach*. Aqualan Press, LLC, 2018. ISBN: 9780998498638.

[10] Alan P. Bowling, Andre F. Palmer, and Lauren Wilhelm. "Contact and Impact in the Multibody Dynamics of Motor Protein Locomotion". In: *Langmuir* 25.22 (2009), pp. 12974–12981.

[11] Alan Bowling and Mahdi Haghshenas-Jaryani. “A multiscale modeling approach for biomolecular systems”. In: *Multibody System Dynamics* 33.4 (Apr. 2015), pp. 333–365.

[12] Alan Bowling and Andre F. Palmer. “The small mass assumption applied to the multibody dynamics of motor proteins”. In: *Journal of Biomechanics* 42.9 (2009), pp. 1218–1223.

[13] Jeremy Q. Broughton et al. “Concurrent coupling of length scales: Methodology and application”. In: *Phys. Rev. B* 60 (4 July 1999), pp. 2391–2403.

[14] Pattabhi R. Budarapu et al. “Efficient coarse graining in multiscale modeling of fracture”. In: *Theoretical and Applied Fracture Mechanics* 69 (2014), pp. 126–143.

[15] Yongyin Cao et al. “Equilibrium orientations and positions of non-spherical particles in optical traps”. In: *Opt. Express* 20.12 (June 2012), pp. 12987–12996.

[16] J.R. Dormand and P.J. Prince. “A family of embedded Runge-Kutta formulae”. In: *Journal of Computational and Applied Mathematics* 6.1 (1980), pp. 19–26.

[17] Robert C. Gauthier and Athanasios Frangioudakis. “Theoretical investigation of the optical trapping properties of a micro-optic cubic glass structure”. In: *Appl. Opt.* 39.18 (June 2000), pp. 3060–3070.

[18] Gérard Gouesbet. “Generalized lorenz-mie theory and applications”. In: *Particle & Particle Systems Characterization* 11.1 (1994), pp. 22–34.

[19] David G. Grier. “A revolution in optical manipulation”. In: *Nature* 424 (Aug. 2003), pp. 810–816.

[20] Honglian Guo et al. “Measurements of leucocyte membrane elasticity based on the optical tweezers”. In: *Chinese Science Bulletin* 48.5 (Mar. 2003), pp. 503–508. ISSN: 1861-9541.

[21] Ashley Guy and Alan Bowling. "A Multiscale Formulation for Reducing Computation Time in Atomistic Simulations". In: *Journal of Computational and Nonlinear Dynamics* 13.5 (Mar. 2018), pp. 051002-051002–9.

[22] M. Haghshenas-Jaryani and A. Bowling. "Multiscale dynamic modeling of processive motor proteins". In: *2011 IEEE International Conference on Robotics and Biomimetics*. Dec. 2011, pp. 1403–1408.

[23] M. Haghshenas-Jaryani and A. Bowling. "Multiscale dynamic modeling of flexibility in myosin V using a planar mechanical model". In: *2012 IEEE International Conference on Robotics and Biomimetics (ROBIO)*. Dec. 2012, pp. 366–371.

[24] Mahdi Haghshenas-Jaryani and Alan Bowling. "A new switching strategy for addressing Euler parameters in dynamic modeling and simulation of rigid multibody systems". In: *Multibody System Dynamics* 30.2 (Aug. 2013), pp. 185–197.

[25] Mahdi Haghshenas-Jaryani and Alan Bowling. "Modeling Flexibility in Myosin V Using a Multiscale Articulated Multi-Rigid Body Approach". In: *Journal of Computational and Nonlinear Dynamics* 10.1 (Oct. 2014), pp. 011015-011015–11.

[26] Mahdi Haghshenas-Jaryani et al. "Dynamics of microscopic objects in optical tweezers: experimental determination of underdamped regime and numerical simulation using multiscale analysis". In: *Nonlinear Dynamics* 76.2 (Apr. 2014), pp. 1013–1030.

[27] Iddo Heller et al. "Optical Tweezers Analysis of DNA–Protein Complexes". In: *Chemical Reviews* 114.6 (2014), pp. 3087–3119.

[28] J. W. J. Kerssemakers et al. "Optical trap setup for measuring microtubule pushing forces". In: *Applied Physics Letters* 83.21 (2003), pp. 4441–4443.

[29] Kurt Kremer and Florian Müller-Plathe. "Multiscale simulation in polymer science". In: *Molecular Simulation* 28.8-9 (2002), pp. 729–750.

[30] U. Lei, C. Y. Yang, and K. C. Wu. "Viscous torque on a sphere under arbitrary rotation". In: *Applied Physics Letters* 89.18 (2006), p. 181908.

[31] Gang Lu, E. B. Tadmor, and Efthimios Kaxiras. "From electrons to finite elements: A concurrent multiscale approach for metals". In: *Physical Review B-Condensed Matter* 73.2 (Feb. 2006).

[32] Martin R. Maxey and James J. Riley. "Equation of motion for a small rigid sphere in a nonuniform flow". In: *The Physics of Fluids* 26.4 (1983), pp. 883–889.

[33] Ali H. Nayfeh. *Perturbation methods*. 1st ed. Pure and applied mathematics. Wiley, 1973.

[34] Keir C. Neuman and Steven M. Block. "Optical trapping". In: *Review of Scientific Instruments* 75.9 (2004), pp. 2787–2809.

[35] Timo A. Nieminen et al. "Optical tweezers: Theory and modelling". In: *Journal of Quantitative Spectroscopy and Radiative Transfer* 146 (2014), pp. 59–80.

[36] Timo A Nieminen et al. "Optical tweezers computational toolbox". In: *Journal of Optics A: Pure and Applied Optics* 9.8 (2007), S196.

[37] CVI Laser Optics. *Gaussian Beam Optics*. URL: https://www.cvilaseroptics.com/file/general/All_About_Gaussian_Beam_OpticsWEB.pdf (visited on 11/03/2018).

[38] Thomas T. Perkins et al. "An interactive optical tweezers simulation for science education". In: vol. 7762. 2010, pp. 776215–7762.

[39] E. M. Purcell. "Life at low Reynolds number". In: *American Journal of Physics* 45.1 (1977), pp. 3–11.

[40] M. S. Rocha. “Optical tweezers for undergraduates: Theoretical analysis and experiments”. In: *American Journal of Physics* 77.8 (2009), pp. 704–712.

[41] G. Roosen. “Optical levitation of spheres”. In: *Canadian Journal of Physics* 57 (Sept. 1979), pp. 1260–1279.

[42] G. Roosen and C. Imbert. “Optical levitation by means of two horizontal laser beams: A theoretical and experimental study”. In: *Physics Letters A* 59.1 (1976), pp. 6–8. ISSN: 0375-9601.

[43] Tamar Schlick. *Molecular Modeling and Simulation: An Interdisciplinary Guide*. 2nd ed. Interdisciplinary Applied Mathematics 21. Springer-Verlag New York, 2010, pp. 489–490. ISBN: 1441963502,9781441963505.

[44] Hossein Talebi, Mohammad Silani, and Timon Rabczuk. “Concurrent multiscale modeling of three dimensional crack and dislocation propagation”. In: *Advances in Engineering Software* 80 (2015), pp. 82–92. ISSN: 0965-9978.

[45] N. B. Viana et al. “Absolute calibration of optical tweezers”. In: *Applied Physics Letters* 88.13 (2006), p. 131110.

[46] N. B. Viana et al. “Towards absolute calibration of optical tweezers”. In: *Phys. Rev. E* 75 (2 Feb. 2007), p. 021914.

[47] Giorgio Volpe and Giovanni Volpe. “Simulation of a Brownian particle in an optical trap”. In: *American Journal of Physics* 81.3 (2013), pp. 224–230.

[48] Qirong Xing et al. “Numerical modeling and theoretical analysis of femtosecond laser tweezers”. In: *Optics & Laser Technology* 36.8 (2004), pp. 635–639.

[49] Q.H. Zeng, A.B. Yu, and G.Q. Lu. “Multiscale modeling and simulation of polymer nanocomposites”. In: *Progress in Polymer Science* 33.2 (2008), pp. 191–269.

BIOGRAPHICAL STATEMENT

Vatsal Asitkumar Joshi was born in Ahmedabad, Gujarat, India, in 1994. He received his B.E. degree from Gujarat Technological University, India, in 2015 and his M.S. degree from The University of Texas at Arlington in 2018 both in Mechanical Engineering. His areas of interest include computational dynamics, robotics, molecular dynamics and controls. Apart from these technical interests, he is a big fan of anime and he enjoys classical Indian and western music.